Title	Theoretical calculation for the multiplet structure of the tetrahedrally coordinated Cr4+ in Y3Al5O12
Author(s)	Ishii, T; Ogasawara, K; Adachi, H; Tanaka, I
Citation	JOURNAL OF CHEMICAL PHYSICS (2001), 115(1): 492-508
Issue Date	2001-07-01
URL	http://hdl.handle.net/2433/39731
Right	Copyright 2001 American Institute of Physics. This article may be downloaded for personal use only. Any other use requires prior permission of the author and the American Institute of Physics.
Type	Journal Article
Textversion	none; publisher

Theoretical calculation for the multiplet structure of the tetrahedrally coordinated Cr^{4+} in $Y_3Al_5O_{12}$

Takugo Ishii,[a] Kazuyoshi Ogasawara, and Hirohiko Adachi
Department of Materials Science and Engineering, Kyoto University, Sakyo-ku, Kyoto 606-8501, Japan

Isao Tanaka
Department of Energy Science and Technology, Kyoto University, Sakyo-ku, Kyoto 606-8501, Japan

(Received 20 December 2000; accepted 11 April 2001)

The multiplet structure of the tetrahedrally coordinated Cr^{4+} in $Y_3Al_5O_{12}$ [yttrium aluminum garnet (YAG)] was calculated by the *ab initio* electronic-structure calculation method. The authors examined the dependence of the multiplet structures on the size of cluster models, with the use of $(CrO_4)^{4-}$ (without point charges), $(CrO_4)^{4-}$ (with point charges), $(CrY_6Al_4O_{44})^{54-}$, and $(CrY_{18}Al_{42}O_{148})^{112-}$ models. The covalency of the impurity-level molecular orbitals was analyzed, and it was revealed that the wave functions of the atoms outside the CrO_4 tetrahedron should not be neglected. The validity of the assignment of the peaks in the absorption spectrum written in the literature was evaluated by the calculated magnitude of the spin-orbit splittings and the oscillator strengths of the transitions, which were obtained by the fully relativistic many-electron calculation. The effect of the codopant on the transition probability was also estimated by $(CrCaY_5Al_4O_{44})^{55-}$ models. It was indicated that the nearest Cr–Ca pairs would reduce the symmetry, and could produce some satellite peaks. The mixing of the wave functions of the triplet states was numerically analyzed, and the results were correlated with the transition probability. The traditional nephelauxetic parameter was estimated, and the value 0.51 was obtained. It was confirmed from first principles that the magnitude of the nephelauxetic parameter in some literature was appropriate. [DOI: 10.1063/1.1377013]

I. INTRODUCTION

The tetravalent chromium (Cr^{4+})-doped crystals and glasses have been intensively studied for the application as solid-state laser materials. The absorption and the emission in the near-infrared (NIR) spectral region have been a matter of interest. The first lasing action by the Cr^{4+} center was reported in the chromium-doped Mg_2SiO_4.[1] In that time, the unusual lasing wavelength lead to confusion on the assignment of the lasing center, and the first paper incorrectly reported the center as the Cr^{3+} state. After the discovery of the Cr^{4+} lasing center, many investigations on searching for the other host crystals have been done. One candidate is the yttrium aluminum garnet (YAG), $Y_3Al_5O_{12}$,[2–4] which has been widely used also as the solid-state-laser crystal doped with rare-earth ions. The Cr^{4+}:YAG is now mainly used as a saturable absorber for the *Q*-switch operation.[5,6] Also in the Cr^{4+}:YAG, however, the difficulty on the assignment of the absorption spectrum has been left in question. Until now the representative literature that discussed the confusing peaks is summarized in Table I.[2,4,6–17] In early years, the two broad bands in the NIR ($\approx 10\,000\,cm^{-1}$) and the visible ($\approx 15\,400\,cm^{-1}$) regions had been assigned to the transitions to the different ${}^3T_2(et_2)$ and ${}^3T_1(et_2)$ triplet terms, respectively. But Eilers *et al.* proposed another assignment that both the bands originated from the same ${}^3T_1(et_2)$ triplet term with a large energy splitting.[13]

The largest reason why misunderstanding and ambiguity have been left on making the assignments of absorption spectra would lie in the practical difficulty in traditional theoretical methods. Most theoretical methods for the analyses of the absorption spectra, produced by impurity center, have been based on the crystal field theory or the ligand field theory.[18] In Cr^{4+}:YAG, the Tanabe–Sugano diagram based on the ligand field theory has often been referred to.[4,13] That method was really convenient to quickly overview the multiplet structure, but the energy splitting caused by the low symmetry was absolutely neglected. After Eilers *et al.* proposed a new assignment by the experiments, Brik and Shchekoldin followed the same assignment by the exchange charges model[15] based on the crystal field theory. Riley *et al.* conducted the alternative calculations[16] based on the angular overlap model (AOM),[19] which was fundamentally based on the ligand field theory. It seems crucial that the AOM calculation had been already performed by Kück *et al.*,[11] who obtained the result supporting the older assignment, differing from Riley's. The largest difference between their AOM calculations seems to have originated from their assumptions on the magnitude of the ligand-field parameter e_σ, which was $8000\,cm^{-1}$ by Kück *et al.*, and $13\,585\,cm^{-1}$ by Riley *et al.* This history simply showed us that those semiempirical methods required us to stand on our assumption to determine the adjustable parameters, which lead to the different conclusions.

In order to avoid ambiguity in determining the parameters and to predict electronic structures not yet known, we

[a]Electronic mail: tack@cms.mtl.kyoto-u.ac.jp

TABLE I. The assignment of the peaks that assumed to have originated from the tetrahedrally coordinated Cr^{4+} in the absorption spectrum of Cr:YAG, written in the literature (cm^{-1}).

Refs.	$^3B[^3T_2(et_2)]$	$^3E[^3T_2(et_2)]$	$^3A[^3T_1(et_2)]$	$^3E[^3T_1(et_2)]$	$^1A[^1E(e^2)]$	$^1B[^1E(e^2)]$
2 (1989)	10 000		15 400			
7 (1989)	10 400		15 600		9090	
8 (1992)	8100	8977, 9281	14 000–26 000			
9 (1992)	8950, 9260					
10 (1994)	7815					
11 (1994)	7814, 7842	9800				
12 (1994)	8100	8977, 9281	14 000–26 000			
13 (1994)	7814		10 000	14 300–16 700	8264, 8292	
4 (1996)	7814, 7842		8977, 9281	15 400		
14 (1997)	7814					
15 (1998)	7814	10 000	9285	16 100		
16 (1999)	7814, 7842	10 000	8977, 9281	15 000	9500 (calc)	
17 (2000)		9990	8977, 9281	14 705		
6 (2000)			8696–12500			

have to depend on *ab initio* methods. In Cr^{4+}:YAG, only a few studies have been done by the *ab initio* electronic-structure calculation methods. Sobolev *et al.* discussed the valence state of the chromium ion by the cluster method with muffin-tin potential.[20] However, their method was based on a one-electron approximation, and they could not directly discuss the multiplet structure derived from the so-called $d-d$ transition, which should be considered by a many-electron calculation. Nowadays, since the speed of computers became fast, Xu and Ching succeeded in completing the band calculation for the YAG host crystal.[21] Ching *et al.* further proposed the model concerning the excited-state absorption in Cr^{4+}:YAG.[22] The band method was powerful and widely accepted, but it also lied under the one-electron approximation, and they did not directly discuss the transitions within the multiplet structure. Regarding the other crystals, only a few studies were indeed reported on the calculations of the multiplet structure of the Cr^{4+} state. In the Cr^{4+}-doped Mg_2SiO_4 and Ca_2GeO_4, Wissing *et al.* conducted the multiplet calculations by using the ADF code,[23] which was a molecular orbital (MO) method based on the density functional theory.[24] Deghoul *et al.* also conducted the calculations by the same code in Cr^{4+}:$LiNbGeO_5$.[25] Their procedure for the multiplet calculations, however, was fundamentally based on the matrix elements obtained by the ligand field theory. Although they could give the mean energies of the multiplet terms, like the Tanabe–Sugano method did, they could not at all obtain the energy splittings within the multiplet terms under the low symmetries, which were indeed in question. Furthermore, the discussion on the transition probability has been absent.

We have been developing a general *ab initio* method, the discrete variational multielectron (DVME) method,[26] for the direct calculations of multiplet structures, independent of the traditional ligand field theory. As for the Cr^{4+}-doped system, we had already confirmed that the method reproduced the absorption spectrum of Cr^{4+}:Ca_2GeO_4, with the large energy splittings and the polarization dependence originating from the low C_s symmetry at the Cr^{4+} site.[27]

In this paper, we report on the results obtained by the *ab initio* calculations for the multiplet structure of the tetrahedrally coordinated Cr^{4+} in the YAG crystal. First, we discuss the one-electron electronic structures obtained from four cluster models with different sizes. Then we compare them with the results obtained from the band calculation by Xu and Ching. The covalency concerning the impurity-chromium levels is then analyzed numerically. Regarding the multiplet calculations, three approaches for the calculation of the matrix elements, concerning the one-electron operator term in the effective many-electron Hamiltonian, are compared with each other, and the newly proposed configuration-independent approach will be concluded to have given the appropriate results. By the results, we show from first principles that the revised assignment of the absorption spectrum proposed by Eilers *et al.* was valid at least with regard to that of the two bands in the NIR and the visible regions concerned the states attributed to the same $^3T_1(et_2)$ triplet term of the tetrahedrally coordinated Cr^{4+}. The transition probability of some transitions between the triplet states will be explained by the analyzed result of the mixing of the wave functions. A result, obtained by a fully relativistic calculation, is shown to discuss the assignment of the peaks in the absorption spectrum in detail. The effect of the formation of Cr–Ca pairs is also briefly discussed. Finally, the traditional nephelauxetic parameter, which expresses the reduction of the electron repulsion in solids, will be estimated from first principles.

II. METHOD

A. The DVME method

1. The general procedure

Since the explanations of the DVME method with the detail mathematical formulation have already been written in Ref. 26, only the descriptions needed to discuss the results in this paper are explained in this section. In this study, the configuration-independent approach and the fully relativistic calculation were additionally introduced. They will be described after this subsection. We first overview the common procedure.

As the first step, a one-electron MO calculation based on the SCAT code[28] is conducted. The MO method is performed within the framework of the density functional theory.[24] The applied exchange potential is $X\alpha$,[29] whose constant α is set at 0.7 as the generally accepted value. The calculation is conducted with the use of a cluster model, in which the information of crystal structure and the symmetry is included. The pth MO φ_p is expressed as the linear combination of the atomic orbitals χ, such as

$$\varphi_p(\mathbf{r}) = \sum_q c_{pq}\chi_q(\mathbf{r}), \tag{1}$$

where $\mathbf{r}$ is the position of electron, and c_{pq} is the coefficient of the linear combination. The coefficients are determined by the self-consistent MO calculation.

Once we obtained the MOs and the one-electron MO energies, we construct the many-electron wave functions as a linear combination of Slater determinants Φ. The ith wave function Ψ_i of the N-electron system (d^N many-electron system in the case of the transition-metal system) is expressed as follows:

$$\Psi_i(\mathbf{r}_1,\mathbf{r}_2,\ldots,\mathbf{r}_N) = \sum_{j=1}^{s} C_{ij}\Phi_j(\mathbf{r}_1,\mathbf{r}_2,\ldots,\mathbf{r}_N),$$

$$\Phi_j(\mathbf{r}_1,\mathbf{r}_2,\ldots,\mathbf{r}_N) = \frac{1}{\sqrt{N!}}\begin{vmatrix} \varphi_{j1}(\mathbf{r}_1) & \varphi_{j2}(\mathbf{r}_1) & \cdots & \varphi_{jN}(\mathbf{r}_1) \\ \varphi_{j1}(\mathbf{r}_2) & \varphi_{j2}(\mathbf{r}_2) & \cdots & \varphi_{jN}(\mathbf{r}_2) \\ \cdots & \cdots & \cdots & \cdots \\ \varphi_{j1}(\mathbf{r}_N) & \varphi_{j2}(\mathbf{r}_N) & \cdots & \varphi_{jN}(\mathbf{r}_N) \end{vmatrix}, \tag{2}$$

where s is the total number of Slater determinants, and C_{ij} is the coefficient of the linear combination. We can make the Slater determinants whose components are the impurity-level MOs, the valence MOs, and the MOs of the conduction band. In this study, we take only the impurity-level MOs that are composed mainly of the Cr $3d$ orbitals, to complete the calculations within a practical period by the contemporary personal computers. We obtain $N=2$ and $s=45$, in the case of Cr^{4+} in this study. Since the linear combination of Slater determinants is composed of the MOs obtained from the MO calculation based on the density functional theory, the DVME method is a hybridized method of the density functional theory and the configuration interaction method. All the configuration interactions concerning the intraconfigurational transition ($d-d$ transition) are fully considered. The effective Hamiltonian H_{eff} of the N-electron system is written in atomic units as

$$H_{\mathrm{eff}}(\mathbf{r}_1,\mathbf{r}_2,\ldots,\mathbf{r}_N) = \sum_{i=1}^{N}\left\{-\frac{1}{2}\nabla_i^2 - \sum_\nu \frac{Z_\nu}{|\mathbf{r}_i-\mathbf{R}_\nu|} + V_0(\mathbf{r}_i)\right\} + \sum_{i=1}^{N}\sum_{j>i}^{N}\frac{1}{|\mathbf{r}_i-\mathbf{r}_j|}, \tag{3}$$

where the first brace is the one-electron operator term and the last term is the two-electron operator term. In the one-electron operator term, the first and the second terms express the kinetic energy and the electron–nuclei (with the atomic number Z) attractive potential of the N electrons, respectively, and the potential V_0 expresses the Coulomb and the exchange interactions between the N electrons and the other core-and-valence electrons. On the other hand, the two-electron operator term expresses the Coulomb repulsion between the N electrons in the impurity-level MOs. In general, the following two-electron integrals have to be calculated to obtain the matrix elements of the two-electron operator term

$$\int\int \phi_i^*(\mathbf{r}_1)\phi_j^*(\mathbf{r}_2)\frac{1}{|\mathbf{r}_1-\mathbf{r}_2|}\phi_k(\mathbf{r}_1)\phi_l(\mathbf{r}_2)d\mathbf{r}_1\,d\mathbf{r}_2, \tag{4}$$

where ϕ is usually considered to be an atomic orbital. The traditional methods based on the ligand field theory transform those integrals into one or two adjustable parameters, such as the Racah parameters B and C, whose values should be determined by referring to experimental data.[18] In the DVME method, the calculation of the two-electron integrals is performed numerically, not analytically, with the use of the MOs, such as

$$C\sum_{r=1}^{\Gamma}\sum_{s>r}^{\Gamma}\varphi_i^*(\mathbf{r}_r)\varphi_j^*(\mathbf{r}_s)\frac{1}{|\mathbf{r}_r-\mathbf{r}_s|}\varphi_k(\mathbf{r}_r)\varphi_l(\mathbf{r}_s)\omega(\mathbf{r}_r)\omega(\mathbf{r}_s), \tag{5}$$

where ω is the weighted volume at each sample point $\mathbf{r}$, and Γ is the number of sample points. The factor C, which is not an empirical parameter, is explained below. This numerical procedure makes it possible to apply the method universally to any symmetry and to any electron configuration. Furthermore, the numerical integration would have a practical benefit that the calculations can be completed within a shorter period than the other methods using the analytical bases, when the order of Slater determinants increased. Finally in the procedure of the DVME method, the energies and the wave functions of the N-electron system are obtained by the diagonalization of the matrix of the effective many-electron Hamiltonian.

Since the number of Slater determinants is finite the electron repulsion, expressed by Eq. (4), should be overestimated due to the insufficient consideration of the correlation effect between the N electrons. To involve the electron-correlation effect, the two-electron integrals in Eq. (5) are multiplied by a correlation-correction factor C, which is straightforwardly determined by a spin-polarized MO calculation. The factor C is determined to satisfy the consistency between the spin-flip transition energy $\Delta\epsilon$, calculated by a one-electron calculation under the transition-state method proposed by Slater,[30] and the corresponding transition energy ΔE, estimated by the N-electron calculation. For example, in the case of the Cr^{4+} state in T_d symmetry, the condition is written as

$$\overline{E[{}^1E,{}^1A_1,{}^3A_2(e_\uparrow e_\downarrow)]} - E[{}^3A_2(e_\uparrow^2)] = \Delta\epsilon(e_\uparrow{}^{1.5}e_\downarrow{}^{0.5}), \tag{6}$$

where all the multiplet states in the square brackets belong to the e^2 electron configuration. The so-called nephelauxetic effect, which means the reduction of the electron repulsion in solids compared to an isolated ion, is expressed in the DVME method by the two factors: the covalency described

as an MO construction [the mixing of the atomic orbitals described by Eq. (1)], and the correlation-correction factor C.

To obtain a theoretical absorption spectrum, the oscillator strength of electric-dipole transition I_{fi} is calculated by

$$I_{fi}=2(E_f-E_i)\left|\int\cdots\int \Psi_f^*\sum_{j=1}^{N}\mathbf{r}_j\cdot\frac{\mathbf{E}}{|\mathbf{E}|}\Psi_i d\mathbf{r}_1\, d\mathbf{r}_2\cdots d\mathbf{r}_N\right|^2, \tag{7}$$

where the subscripts i and f mean the initial and the final states, respectively, E_i and E_f are their energies, and $\mathbf{E}$ is the electric field of incident light. A theoretical spectrum is obtained by applying the oscillator strength to the Lorentz resonance curve with a full width at half maximum of 325 cm^{-1}. We note that we can discuss the peak energy and the intensity in absorption spectra, but could not yet discuss the peak width. The theoretical spectra will be shown in order to easily compare the calculated results with the experimentally obtained absorption spectrum.

2. The configuration-dependent and-independent approaches

In this study, we compare three approaches for the calculation of the matrix elements concerning the one-electron operator term in the effective many-electron Hamiltonian. The three approaches are the Fazzio–Caldus–Zunger (FCZ), the configuration-dependent correction (CDC), and the configuration-independent correction (CIC) approaches. The FCZ and the CDC approaches were already introduced in Ref. 26, and the CIC approach is introduced in this paper. The FCZ and the CDC approaches are configuration dependent, but on the other hand the CIC approach is configuration independent. Here ''configuration'' means the electron configuration that can be determined from one-electron MO energy. For example, in the case of the Cr^{4+} ion in T_d symmetry, the impurity levels split into the two states with e and t_2 symmetries. We can define an effective ligand-field splitting Δ_{eff} from the energy difference between the two states such as

$$\Delta_{\mathrm{eff}}=\overline{\varepsilon(t_2)}-\overline{\varepsilon(e)}, \tag{8}$$

where ε is the MO energy, and the attached overline means to take an average value when the degenerate states further split into several states in the lower symmetry than the T_d symmetry. Then the electron configurations are $e^m t_2^n;(m,n)=(2,0),(1,1),(0,2)$, and their mean energies are obtained by

$$n\Delta_{\mathrm{eff}}. \tag{9}$$

In the FCZ approach, the diagonal matrix elements are determined so that the mean energy of every electron configuration is consistent with Eq. (9), and the multiplet splitting, originating from the electron repulsion [Eq. (4)] can be considered to be a splitting from the mean energy. This description is based on the approach proposed by Fazzio *et al.*[31] The FCZ approach is the simplest approach. The useful aspect of the FCZ approach is that we do not need to know any explicit formula of the potential V_0 in Eq. (3). However, the FCZ approach tends to give the invalid result of the multiplet splittings originating from the reduction of symmetry, as pointed out in Ref. 26.

We concluded in the previous paper that the CDC approach was a good approach in practice. In the CDC approach, the following explicit formula for the potential V_0 in Eq. (3), proposed by Watanabe and Kamimura,[32] is introduced to accurately reproduce both the energy and the polarization dependence:

$$\begin{aligned}V_0(\mathbf{r}_i)=&\int\frac{\rho_0(\mathbf{r})}{|\mathbf{r}_i-\mathbf{r}|}d\mathbf{r}\\&+\frac{3}{4}\frac{\rho_{\mathrm{tot}}(\mathbf{r}_i)V_{\mathrm{xc}}[\rho_{\mathrm{tot}}(\mathbf{r}_i)]-\rho_0(\mathbf{r}_i)V_{\mathrm{xc}}[\rho_0(\mathbf{r}_i)]}{\rho_{\mathrm{imp}}(\mathbf{r}_i)}\\&-V_{\mathrm{xc}}[\rho_{\mathrm{imp}}(\mathbf{r}_i)],\end{aligned} \tag{10}$$

where ρ_{tot}, ρ_0, and ρ_{imp} are the electron densities of all the occupied MOs, the core-and-valence MOs, and the impurity-level MOs, respectively, and the potential V_{xc} is the exchange $X\alpha$ potential. It was revealed that some overestimation was involved in the evaluation of the matrix elements concerning the one-electron operator term. In the CDC approach, the values of diagonal matrix elements are shifted by applying the same procedure as the FCZ approach.

Still the CDC approach is a convenient approach when we really know the electron configurations; we propose another CIC approach, which involves configuration-independent correction for the matrix elements concerning the one-electron operator term. The CIC approach also involves the direct evaluation by Eq. (10). In the CIC approach, all the matrix elements of the one-electron operator term are universally multiplied by a scaling factor D, instead of combining with the configuration-dependent FCZ approach. The scaling factor D mainly concerns the magnitude of ligand-field splitting, and can be determined to either reproduce the experimentally obtained spectrum or obtain the equivalent result to the CDC approach. Therefore the CIC approach with only one scaling factor omits the *ab initio* character from the DVME method, whereas the FCZ and CDC approaches really lie in the framework of the *ab initio* calculation. However, the scaling factor D affects the calculated energies so as only to shift them as a whole, and it does not crucially affect the polarization dependence, which is important in most cases under low symmetry. We can proceed with the calculations, even if the analytical expression for the matrix elements is too complex to be formulated, if we only fix the scaling factor D at a standard value for the system. In practice, we may use the CDC approach when we want to perform a perfect *ab initio* calculation, and we may use the CIC approach when we want to discuss the energy with higher accuracy by adjusting the scaling factor. In the future, we will consider that such technical corrections will not be required when we use spin-polarized MOs, and when we increase the order of Slater determinants.

3. Fully relativistic many-electron calculation

Until now, we performed all the many-electron calculations under a nonrelativistic approximation. Therefore we did not discuss any of the relativistic effects, including the spin-orbit splitting and the energy shift caused by the relativistic contraction. In the case of transition metals, the dominant relativistic effect is only the spin-orbit splitting, and it is enough to neglect even the spin-orbit interaction when we roughly discuss the assignment of the peaks in the absorption spectra, since the magnitude of the spin-orbit splitting is relatively smaller than that of the ligand-field splitting. In this study, however, we extended our discussion on the assignment by conducting a fully relativistic calculation. Here the term 'fully' means that all the relativistic effects were considered by directly solving the Dirac equation. We developed the DVME method based on the fully relativistic SCAT code.[33] This paper is the first one to apply the relativistic many-electron calculation method to the solid-state laser materials. The method will also be applied universally to the heavy rare-earth ion system in the near future.

The overall procedure of the relativistic many-electron calculation is the same as the nonrelativistic one, which was described in the previous subsections. The differences in the relativistic calculation are the expressions of the wave function and the kinetic-energy term in the Hamiltonian. Whereas the atomic orbital χ in Eq. (1) was a simple scalar in the nonrelativistic calculation, it is a relativistic four-component vector with the real components and the imaginary components in the relativistic calculation. The effective many-electron Hamiltonian of the nonrelativistic Schrödinger equation in Eq. (3) is replaced by the relativistic Hamiltonian of the Dirac equation, which is written with the use of the Pauli's matrices, as follows:

$$H_{\mathrm{eff}}(\mathbf{r}_1,\mathbf{r}_2,\ldots,\mathbf{r}_N)=\sum_{i=1}^{N}\left\{-ic\tilde{\boldsymbol{\alpha}}\cdot\boldsymbol{\nabla}+c^2\tilde{\beta}-\sum_{\nu}\frac{Z_\nu}{|\mathbf{r}_i-\mathbf{R}_\nu|}+V_0(\mathbf{r}_i)\right\}+\sum_{i=1}^{N}\sum_{j>i}^{N}\frac{1}{|\mathbf{r}_i-\mathbf{r}_j|},$$

$$\tilde{\boldsymbol{\alpha}}=\begin{pmatrix}\tilde{\mathbf{0}} & \tilde{\boldsymbol{\sigma}}\\ \tilde{\boldsymbol{\sigma}} & \tilde{\mathbf{0}},\end{pmatrix},\quad \tilde{\beta}=\begin{pmatrix}\tilde{I} & \tilde{0}\\ \tilde{0} & -\tilde{I}\end{pmatrix},\qquad (11)$$

$$\tilde{\sigma}_x=\begin{pmatrix}0 & 1\\ 1 & 0\end{pmatrix},\quad \tilde{\sigma}_y=\begin{pmatrix}0 & -i\\ i & 0\end{pmatrix},\quad \tilde{\sigma}_z=\begin{pmatrix}1 & 0\\ 0 & -1\end{pmatrix},$$

$$\tilde{I}=\begin{pmatrix}1 & 0\\ 0 & 1\end{pmatrix},\quad \tilde{0}=\begin{pmatrix}0 & 0\\ 0 & 0\end{pmatrix},$$

where c is velocity of light. The inclusion of the relativistic effects in the DVME method is neither different from the simplest pertubation method, nor from the methods with a scalar relativistic approximation, which has often been applied to the contemporary *ab initio* methods. The results, obtained by the relativistic method, are shown in Sec. III B 2.

B. Cluster models

The YAG crystal belongs to the garnet type structure in the cubic crystal system.[34] The unit cell has 160 atoms (8 f.u.). The yttrium (Y) atom is dodecahedrally coordinated by the oxygen (O) atoms. On the other hand, 2/5 of the aluminum (Al) atoms are octahedrally coordinated and the rest of the Al atoms are tetrahedrally coordinated. Since the ionic radius of Y^{3+} (1.019 Å) is large enough compared to that of Cr ions ($\leqslant$0.615 Å),[35] the Cr atom has been assumed to substitute only for the smaller Al sites. In order to produce the unstable Cr^{4+} state, the Ca^{2+} or Mg^{2+} ion is always codoped in the crystal growth for charge compensation. Several valences, such as Cr^{3+}, Cr^{4+}, and Cr^{6+}, have been considered to coexist in the Cr^{4+}:YAG sample,[7,12,17] but the dominant structure of the absorption spectrum in the NIR–visible region up to about 18 000 cm^{-1} has been assigned to the tetrahedrally coordinated Cr^{4+}.

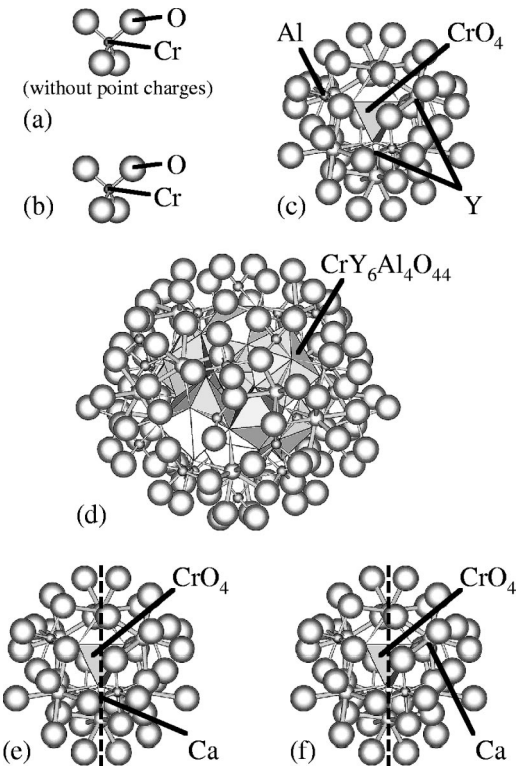

FIG. 1. The cluster models: (a) $(CrO_4)^{4-}$ (without point charges), (b) $(CrO_4)^{4-}$, (c) $(CrY_6Al_4O_{44})^{54-}$, (d) $(CrY_{18}Al_{42}O_{148})^{112-}$, and (e) and (f) $(CrCaY_5Al_4O_{44})^{55-}$ models. The symmetries at the center Cr atoms are D_{2d} in model (a), S_4 in models (b)–(d), C_2 in model (e), and C_1 in model (f). In models (b)–(f), the additional point charges with formal valences are placed at the atomic sites outside the clusters to reproduce the effective Madelung potential.

In this study, we concentrate on the electronic structure of the tetrahedrally coordinated Cr^{4+} state. For the calculations, we used totally six cluster models, which are shown in Fig. 1. Models (a)–(d) are the models without any charge compensators; on the other hand, models (e) and (f) are the models to estimate the effect of the nearest Cr–Ca pairs. The $(CrO_4)^{4-}$ cluster model (a) is the simplest model as often seen in the semiempirical methods. The coordinates of the atoms were taken from the structure of the YAG crystal.[34] The central tetrahedrally coordinated Al atom was replaced by a Cr atom. The Cr site had D_{2d} symmetry, which was expressed by the different O–Cr–O bond angles, $\angle$OCrO $=99.9$ and 114°. The $(CrO_4)^{4-}$ model (b) is an extended

model from model (a). Within the spatial region of $6\times6\times6$ unit cells, additional point charges with formal valences were placed at the atomic sites outside the five atoms to reproduce the effective Madelung potential. As a result, the symmetry at the Cr site was reduced further to S_4, which was the exact symmetry. The $(CrY_6Al_4O_{44})^{54-}$ model (c) is a further extended model from model (b) by adding the atoms around the CrO_4 coordination tetrahedron. The four ligand O atoms around the Cr atom were completely shared by the YO_8 and AlO_6 coordination polyhedra, so that the covalency around the Cr atom is expected to be expressed well. The $(CrY_{18}Al_{42}O_{148})^{112-}$ model (d) is the largest model in this study with 209 atoms. In this model, the atoms, present in the model (c) [drawn by the polyhedra in Fig. 1(d)], were completely surrounded by the bonding coordination polyhedra (drawn by the balls). The distance between the central Cr atom and the farthest metal atom (Al) was 7.04 Å. The cell parameter of the YAG crystal is $a=12.00$ Å, and the model (d) had all the representative sites in the unit cell. The final $(CrCaY_5Al_4O_{44})^{55-}$ models (e) and (f) were based on the model (c), and one Y atom was replaced by one Ca atom. In the model (e), the substituted Y atom was located on the primary axis of the S_4 symmetry, on the other hand, the substituted Y atom was not located on the primary axis in the model (f). The Cr–Ca distances were 3.00 Å in model (e) and 3.67 Å in model (f). The symmetries at the Cr site in models (e) and (f) were reduced to C_2 and C_1, respectively. Actually, we may have to also consider the models with different Cr–Ca separations. We regard models (e) and (f) as the models that produce the largest effect of the Ca codoping.

The atomic orbitals used in the MO calculations were $1s-4p$ for Cr, $1s-2p$ for O, $1s-5p$ for Y, $1s-3d$ for Al, and $1s-4p$ for Ca.

III. RESULTS AND DISCUSSION

A. One-electron MO calculation

1. The one-electron MO energies and the density of states

The calculated one-electron MO energies by the nonrelativistic SCAT code are shown in Figs. 2(a)–2(f) for the cluster models (a)–(f), respectively. The lowest Cr $3d$ level, which two electrons occupied, was set at zero. The MOs of the valence bands were composed of the O $2s$ and O $2p$ orbitals, and were also composed of the Y $4p$ orbitals mixing with the O $2s$ orbitals in the larger models (c)–(f). The MOs of the unoccupied levels (conduction bands) were only composed of the Cr $4s$ and Cr $4p$ orbitals in the small models (a) and (b), however on the other hand, they were mainly composed of the Y $4d$, Y $5s$, Y $5p$, Al $3s$, Al $3p$, and Al $3d$ orbitals in the larger models (c)–(f). In the results obtained from the models (e) and (f), the additional Ca $3p$ levels were located at the top of the O $2s$ valence band, and the Ca $3d$ levels were located in the higher energy region than the Y $4d$ unoccupied band. In all the models, the discrete impurity levels, whose MOs were mainly composed of the Cr $3d$ orbitals, were located between the valence O $2p$ band and the unoccupied levels. The impurity levels split into four or five

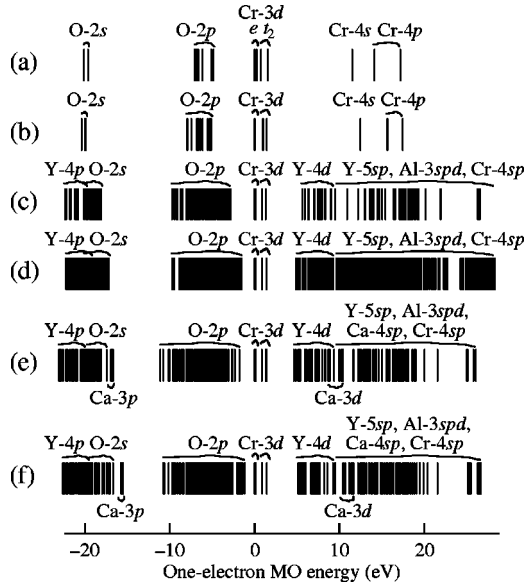

FIG. 2. The calculated one-electron MO energies obtained from cluster models (a)–(f). The lowest Cr $3d$ impurity level is set at zero.

levels by the ligand field under the low symmetries. The symmetry of those impurity-level MOs, in the order of their energies, were b_1, a, b_2, and e in model (a), b, a, b, and e in models (b)–(d), a, a, a, b, and b in model (e), and all a in model (f). Since the e state was twofold degenerate, we obtained five totally impurity-level MOs from every model. We hereafter specify those impurity-level MOs by attaching the labels with the figures expressing the order of the energies, for example, $b_{1(1)}$, $a_{(2)}$, $b_{2(3)}$, $e_{(4)}$, and $e_{(5)}$ in the case of model (a). The five impurity-level MOs were chosen as the components of the Slater determinants in Eq. (2). In the parent T_d symmetry, the MOs with the labels (1) and (2) are twofold degenerate with e symmetry, and the MOs with the labels (3), (4), and (5) are threefold degenerate with t_2 symmetry. In all the results, however, the apparent energy splittings between the MOs with label (3) and the MOs with labels (4) and (5) were observed, and the magnitude of the splitting ranged from 0.42 eV [model (e)] to 0.72 eV [model (a)]. Although the energy splitting of the MOs originating from the t_2 symmetry was large, we still use the notations e and t_2 in the T_d symmetry when we specify the electron configurations. Then we can define an effective ligand field splitting Δ_{eff} according to Eq. (8). The calculated values of the Δ_{eff} for models (a), (b), (c), (d), (e), and (f) were 1.19, 1.27, 1.16, 1.15, 1.14, and 1.13 eV, respectively. The value of the model (b) was about 0.1 eV larger than the others.

The result, obtained from the smallest model (a) in Fig. 2(a), showed the largest energy splitting within the impurity levels among the four models. In the result obtained from model (b) in Fig. 2(b), the energy splittings decreased. On the contrary, the bandwidth of the valence O $2p$ band became larger. Those indicate that the point charges, placed outside the cluster in model (b), further produced the difference of the potentials at the different ligand O atoms, and as a result, the energy splittings were relaxed. In models (a) and (b), the Cr $3d$ orbitals in the impurity-level MOs are expected to interact with the O $2p$ orbitals, which were the

nearest states in energy. In the result obtained from the larger model (c) in Fig. 2(c), the impurity levels were sandwiched between the valence O $2p$ band and the conduction band, whose lowest MO components were the Y $4d$ orbitals. In that case, the impurity-level MOs are expected to be composed not only of the Cr $3d$ and O $2p$ orbitals, but also of the Y $4d$ orbitals. In the result obtained from model (d) in Fig. 2(d), the total structure did not qualitatively change from that of model (c), but the conduction band became continuous. However, the impurity-level energies did not significantly change. So we can expect that the multiplet structures, obtained from models (c) and (d), will not significantly differ from each other. The calculated values of the band gap, obtained from models (c) and (d), were 8.44 and 6.45 eV, respectively. The value shown in the literature was 6.5 eV.[36,37] Xu and Ching reported the value 4.71 eV by the band method,[21] which involved the general local-density approximation, leading to the underestimation similar to the $X\alpha$ approximation. In this study, the MO method involved a cluster approximation, which tended to overestimate the magnitude of the band gap. In the calculated result obtained from model (d), the underestimation due to the $X\alpha$ approximation and the overestimation due to the cluster approximation fortunately canceled each other out, and resulted in a good agreement with the experimentally obtained value. We consider, however, the magnitude of the band gap to be less important than that of the energy splitting within the impurity levels, since we concentrate only on the discrete impurity levels that were isolated from both the top of the valence band and the bottom of the conduction band. In the results obtained from models (e) and (f), the additional Ca $3p$ and Ca $3d$ levels participated in the energy structures. However, the Ca $3p$ levels lay below the O $2p$ valence band, and the Ca $3d$ levels lay above the Y $4d$ unoccupied band. Since their energy separations between the Cr $3d$ levels were large, the direct interaction between the Ca orbitals and the Cr $3d$ orbitals is expected to be small. The energy splittings of the Cr $3d$ levels also did not significantly change from those of model (c) without the Ca charge compensator.

In general, the band method gives the better electronic structure of the infinite system than the cluster method. To compare the results of our MO method and Xu's band method,[21] the total density of states (DOS) and the partial DOS (PDOS), attributed to the Y, Al, and O atoms, were depicted in Figs. 3(a), 3(b), and 3(c). Figures 3(a) and 3(b), which were obtained from our larger models (c) and (d), correspond to the results shown in Figs. 2(c) and 2(d), respectively. The total DOS and the PDOS were determined by applying the calculated MO energies and the populations, obtained by the Mulliken's population-analysis method,[38] to the Gaussian curve with a full width at half maximum of 0.5 eV. The concentration of the Cr atom was set at 0.2 at %, and the contribution of the Cr atom to the results was negligibly small. For Xu's PDOS of the Al atom in Fig. 3(c), we took only the result of the Al atom at the octahedrally coordinated site but not at the tetrahedrally coordinated site, since the overall structures resembled each other for a rough comparison with our results. In order to regard the PDOS of the octahedrally coordinated Al atom as the total PDOS of the

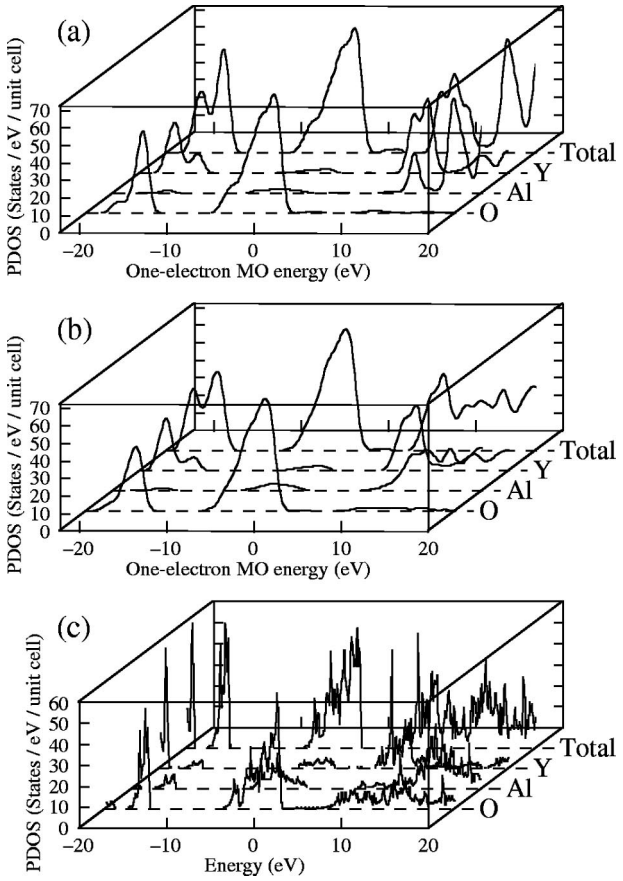

FIG. 3. The total DOS and the PDOS attributed to the Y, Al, and O atoms, obtained from (a) the model (c), (b) the model (d), and (c) Ref. 21. In (a) and (b), the DOS and the PDOS were obtained by applying the calculated MO energies and the populations to the Gaussian curve with a full width at half maximum of 0.5 eV. The concentration of the Cr atom was set at 0.2 at %.

Al atom, the absolute values of the PDOS were multiplied by 5/2, different from the values in the original Ref. 21. The origins of the energy in all the figures were set at the highest levels in the valence O $2p$ bands. Comparing our results in Figs. 3(a) and 3(b), we see that their conduction bands differed from each other, whereas the difference between their valence bands was small. The conduction band of the smaller model (c) showed the rather discrete structure, in which each Y $4d$, Al $3s$, and Al $3p$ band was resolved well. On the other hand, the conduction band of the largest model (d) showed the continuous structure. Nevertheless, the Y $4d$ band at the bottom was distinct from the Al bands located in the higher energy region. Comparing the result of model (d) in Fig. 3(b) with Xu's in Fig. 3(c), we see that the agreement between them was good. The Y p band was located at the lowest energy, and soon above that, the O s band was located. The valence O p band spread within the energy range from -10 to 0 eV, and the bottom of the unoccupied band was composed of the Y d band. The Al bands were located at the higher energy region. We conclude from the agreement that our calculated MOs appropriately reproduced the electronic structure of the host YAG crystal. Since the overall band positions did not significantly change between the results obtained from models (c) and (d), we consider that the

TABLE II. The results of the Mulliken's population analyses obtained from models (a)–(f).

		Cr		Ligand O		Y		Al	Ca
	MO	$3d$	$4s+4p$	$2s$	$2p$	$4d$	$4p+5s+5p$	$3s+3p+3d$	$3d+4s+4p$
(a)	$b_{1(1)}(e)$	0.837	0.000	0.000	0.163	⋯	⋯	⋯	⋯
	$a_{(2)}(e)$	0.833	0.009	0.000	0.159	⋯	⋯	⋯	⋯
	$b_{2(3)}(t_2)$	0.748	0.040	0.005	0.206	⋯	⋯	⋯	⋯
	$e_{(4)\&(5)}(t_2)$	0.718	0.054	0.008	0.220	⋯	⋯	⋯	⋯
(b)	$b_{(1)}(e)$	0.874	0.000	0.000	0.126	⋯	⋯	⋯	⋯
	$a_{(2)}(e)$	0.858	0.003	0.000	0.139	⋯	⋯	⋯	⋯
	$b_{(3)}(t_2)$	0.764	0.037	0.007	0.191	⋯	⋯	⋯	⋯
	$e_{(4)\&(5)}(t_2)$	0.746	0.043	0.009	0.201	⋯	⋯	⋯	⋯
(c)	$b_{(1)}(e)$	0.840	0.000	0.000	0.126	0.009	0.003	0.013	⋯
	$a_{(2)}(e)$	0.801	0.004	0.000	0.168	0.007	0.000	0.007	⋯
	$b_{(3)}(t_2)$	0.729	0.043	0.004	0.189	0.020	0.001	0.005	⋯
	$e_{(4)\&(5)}(t_2)$	0.713	0.049	0.009	0.186	0.010	0.003	0.020	⋯
(d)	$b_{(1)}(e)$	0.836	0.000	0.000	0.123	0.010	0.003	0.014	⋯
	$a_{(2)}(e)$	0.798	0.004	0.000	0.165	0.008	0.001	0.008	⋯
	$b_{(3)}(t_2)$	0.722	0.043	0.004	0.182	0.025	0.001	0.008	⋯
	$e_{(4)\&(5)}(t_2)$	0.705	0.050	0.008	0.182	0.012	0.003	0.023	⋯
(e)	$a_{(1)}(e)$	0.844	0.000	0.000	0.123	0.010	0.001	0.013	0.000
	$a_{(2)}(e)$	0.805	0.006	0.000	0.163	0.008	0.000	0.008	0.000
	$a_{(3)}(t_2)$	0.728	0.040	0.003	0.195	0.018	0.001	0.005	0.002
	$b_{(4)}(t_2)$	0.733	0.043	0.009	0.170	0.013	0.002	0.021	0.000
	$b_{(5)}(t_2)$	0.701	0.056	0.009	0.189	0.012	0.002	0.022	0.000
(f)	$a_{(1)}(e)$	0.843	0.000	0.001	0.125	0.008	0.002	0.012	0.001
	$a_{(2)}(e)$	0.803	0.004	0.000	0.164	0.008	0.000	0.007	0.000
	$a_{(3)}(t_2)$	0.733	0.043	0.004	0.182	0.023	0.001	0.005	0.000
	$a_{(4)}(t_2)$	0.722	0.047	0.009	0.180	0.011	0.002	0.020	0.000
	$a_{(5)}(t_2)$	0.707	0.050	0.008	0.194	0.008	0.001	0.019	0.002

result of the smaller model (c) also essentially reproduced the band structure.

2. The covalency of impurity-level MOs

The Coulomb repulsion between the electrons in the d orbitals of an isolated transition-metal ion is greatly reduced when the ion formed bonds connected with the surrounding atoms in solids. We considered the reduction by the two factors: one is the effect of the covalency, which was estimated by the proportions of the contribution of the Cr $3d$ orbitals to the impurity-level MOs, and the other is the correlation correction, which was expressed by the correlation-correction factor C in Eq. (5). In nature, both the factors are not adjustable parameters, and are estimated straightforwardly within the computational procedure.

We evaluated the covalency of the impurity-level MOs by the Mulliken's population-analysis method,[38] which quantifies the contribution of the atomic orbitals to an MO, summarizing the coefficients c_{pq} in Eq. (1). The results of the analyses by the nonrelativistic calculations are shown in Table II for models (a)–(f). The contributions were classified into the Cr $3d$, Cr $(4s+4p)$, ligand (first-nearest) O $2s$ and O $2p$, Y $4d$, Y $(4p+5s+5p)$, Al $(3s+3p+3d)$, and Ca $(3d+4s+4p)$ orbitals. For the larger models (c)–(f), the components of the O atoms outside the CrO_4 coordination tetrahedron were not explicitly listed.

In all the impurity-level MOs, the primary component was the Cr $3d$ orbitals, which mainly mixed with the ligand O $2p$ orbitals. The proportion of the contribution of the Cr $3d$ orbitals was less than 0.88. The decrease of the contribution of the Cr $3d$ orbitals can be regarded as a degree of covalency. Since the degree of covalency was large, the electron configuration should be actually written as $(CrO_4)^{4-}$, $(CrY_6Al_4O_{44})^{54-}$, and so on, instead of being written as d^2, based on the simplest atomic notation. We see from Table II that the proportions of the contribution of the Cr $3d$ orbitals to the MOs, originating from t_2 symmetry, were about 0.1 smaller than the MOs originating from e symmetry. This difference forced the traditional methods based on the ligand field theory to introduce more than one adjustable parameter (e_σ and e_π in the AOM method). In the result obtained from the smallest model (a), the difference between the $b_{(1)}$ and $a_{(2)}$ states originating from e symmetry was small, whereas the difference in the other models with additional point charges was significantly large. On the contrary, the corresponding one-electron MO energies, obtained from model (a) in Fig. 2(a), had the largest energy splitting at 0.30 eV. This indicates that we cannot judge the component of the MOs only from whether the one-electron MO energies look degenerate or not. Comparing the results of the models (a) and (b), we see that the contribution of the Cr $3d$ orbitals in model (b) was larger than that in model (a), indicating that the Cr atom in model (b) had stronger ionic character than

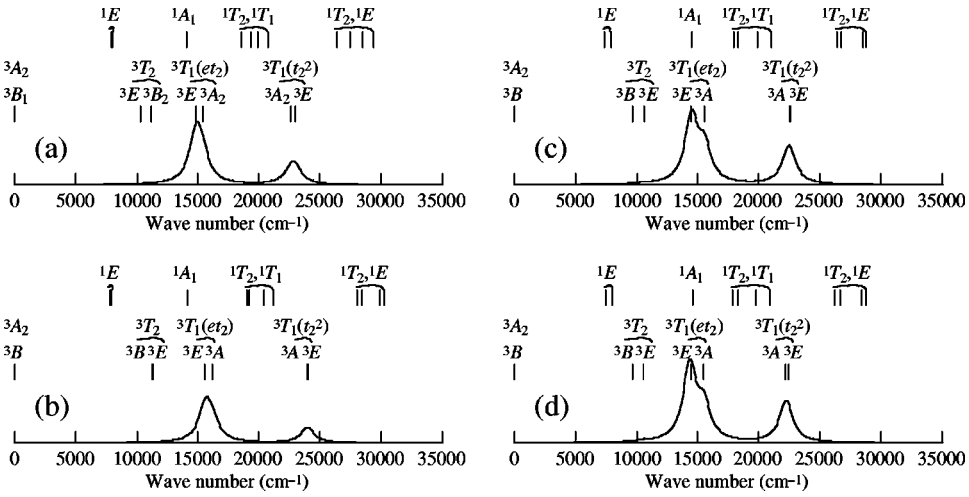

FIG. 4. The calculated multiplet energies and the theoretical absorption spectra obtained from models (a)–(d) by the FCZ approach.

model (a). The largest repulsion between the electrons in the impurity-level MOs is expected in model (b). Moving to the result of model (c), we see that the proportions of the contribution of the Cr $3d$ orbitals were reduced by the participation of the additional cations' orbitals, mainly, the Y $4d$ and Al orbitals. This means that the existence of the cations' orbitals outside the CrO_4 coordination tetrahedron should not be neglected. Comparing the results obtained from models (c) and (d), we could not see any large difference between them. Summarizing the dependence of the size of the cluster models, we conclude that the $(CrO_4)^{4-}$ models (a) and (b) are not sufficient, but the $(CrY_6Al_4O_{44})^{54-}$ model (c) with complete packing of the CrO_4 tetrahedron by the cations' coordination polyhedra of the first shell is practically sufficient for the description of the impurity-level MOs. By the results obtained from models (e) and (f), we can discuss the effect of the formation of the nearest Cr–Ca pairs. We see from Table II that the MOs originating from t_2 symmetry split into three states by the reduction of the symmetry to C_2 or C_1, and the compositions of the Cr $3d$ and O $2p$ orbitals were accordingly changed. This change in the covalency must affect the multiplet structures. Regarding the Ca orbitals, the contribution was negligible. This is natural because the energy difference between the Cr $3d$ and Ca $3d$ levels was larger than the energy difference between the Cr $3d$ and Y $4d$ levels, as shown in the previous subsection. The absence of the direct interaction between the Cr and Ca atoms means that the Ca atom acted like as an isolated ion for the impurity levels. On the other hand, the mean proportions of the contribution of the other atoms, including the Y atoms, did not significantly differ from the result of model (c) without the Ca atom. Considering the decrease in the number of Y atoms from six to five, we can conclude that the net overlap between the Cr atom and every Y atom increased in models (e) and (f). This means that the so-called backbond was formed, that is, the lost Cr–Y bond was compensated by strengthening the other Cr–Y bonds. Although the Ca orbitals did not directly participate in the impurity-level MOs, it changed the MOs to enhance the effect of the reduction of the symmetry by creating the backbonds.

Let us compare the contribution of the Cr $3d$ orbitals in Table II with the results in Ref. 26, where the Cr^{3+} and V^{3+} at the octahedrally coordinated site in α-Al_2O_3 were responsible for the impurity absorptions. In the case of the octahedrally coordinated Cr^{3+} (ruby), the proportions of the contribution of the Cr $3d$ orbitals to the impurity-level MOs were 0.91 and 0.81 for the MOs originating from t_{2g} and e_g symmetries, respectively. Almost the same values, 0.90 and 0.80, were obtained for the octahedrally coordinated V^{3+}, whose number of electrons occupying the impurity-level MOs was the same as Cr^{4+}. The corresponding values in Table II for the tetrahedrally coordinated Cr^{4+} were smaller by 0.04–0.11. This means that the covalency concerning the impurity-level MOs of the tetrahedrally coordinated Cr^{4+} is much stronger than the covalency of the octahedrally coordinated Cr^{3+}, and that the degree of covalency was determined by the coordination number.

B. Multiplet structure calculations

1. The multiplet energies and the transition probabilities by the three approaches

In this subsection, we mainly discuss the methodological aspects, and confirm roughly the validity of the assignment of the absorption spectrum proposed by Eilers *et al.* We examined the dependence of the calculated multiplet energies and the transition probabilities on the size of the cluster models, with the models (a)–(d) by the nonrelativistic calculations. With every cluster model, we conducted the calculations by the FCZ, the CDC, and the CIC approaches. In the calculations by the CIC approach, the scaling factor D was fixed at 0.8. Although the factor C can be calculated from first principles, we obtained it by fixing the $\Delta\epsilon$ in Eq. (6) at an average value 0.93 eV through the calculations for simplification. The calculated multiplet energies and the theoretical spectra, obtained from models (a)–(d) by the FCZ, the CDC, and the CIC approaches, are shown in Figs. 4, 5, and 6, respectively. In all the figures, the calculated multiplet energies were classified into the singlet states (upper) and the triplet states (lower), shown as straight lines. The ground state was set at zero. The levels were shown up to $35\,000\,cm^{-1}$. The multiplet-term symbols in the parent T_d symmetry were attached to the levels. The triplet states had the $^3A_2$ ground-state term, the $^3T_2$ and $^3T_1$ terms in the one-

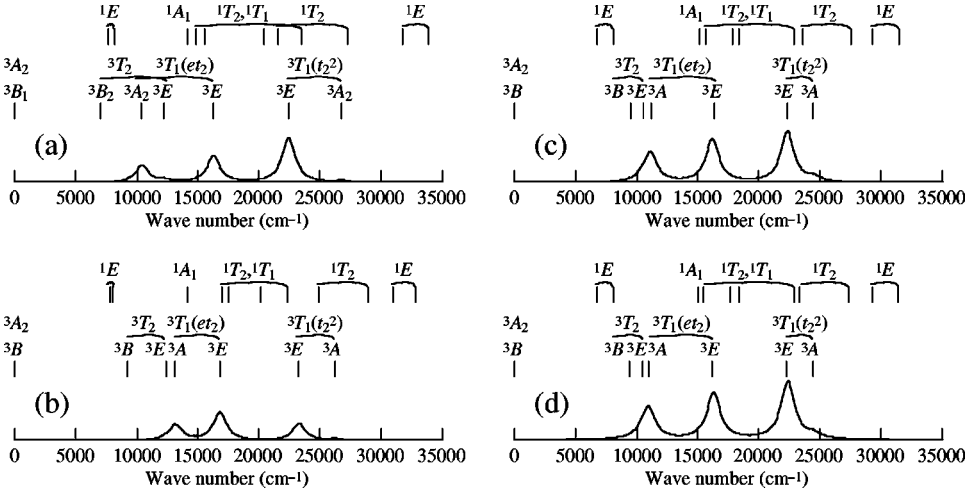

FIG. 5. The calculated multiplet energies and the theoretical absorption spectra obtained from models (a)–(d) by the CDC approach.

electron-excited electron configuration (et_2), and the $^3T_1$ term in the two-electron-excited electron configuration (t_2^2). The multiplet-term symbols in the exact D_{2d} symmetry [model (a)] or the S_4 symmetry [models (b)–(d)] were also attached to the triplet states, on which we concentrate. In the results obtained from model (a), the ground state was $^3B_1$, and we denote it as $^3B_1[^3A_2]$ to also realize the origin in the parent T_d symmetry. In the same way, the excited triplet states were denoted as $^3E[^3T_2]$, $^3B_2[^3T_2]$, $^3A_2[^3T_1(et_2)]$, $^3E[^3T_1(et_2)]$, $^3E[^3T_1(t_2^2)]$, and $^3A_2[^3T_1(t_2^2)]$. In the results obtained from models (b)–(d), the ground state was the $^3B[^3A_2]$ state, and the excited triplet states were $^3B[^3T_2]$, $^3E[^3T_2]$, $^3A[^3T_1(et_2)]$, $^3E[^3T_1(et_2)]$, $^3E[^3T_1(t_2^2)]$, and $^3A[^3T_1(t_2^2)]$. In the lower field in Figs. 4, 5, and 6, the theoretical absorption spectra were depicted. The theoretical spectra were obtained by Eq. (7), where the initial state was the ground state, and the final state was all the excited triplet states. The relative height of the spectra was preserved through the figures, and can be compared between them.

In Fig. 6(e), the experimentally obtained absorption spectrum, obtained by Kück *et al.*,[4] is shown for comparison with the theoretical spectra. The experimentally obtained spectrum had mainly three broad bands peaking at about 1000 nm (10 000 cm^{-1}) in the NIR region, and at around 650 nm (15 400 cm^{-1}) and 450 nm (22 200 cm^{-1}) in the visible region. Kück *et al.* followed the assignment proposed by Eilers *et al.*,[13] and attributed the former two bands at 10 000 and 15 400 cm^{-1} to the transitions from the $^3B_1(^3A_2)$ ground state to the $^3A_2(^3F)$ and $^3E(^3F)$ excited states, respectively, which corresponded to the $^3A[^3T_1(et_2)]$ and $^3E[^3T_1(et_2)]$ excited states by our expression based on the MO framework in the S_4 symmetry. Kück *et al.* indicated by the excitation spectrum that the $^3T_1(t_2^2)$ states lay in the 300–500 nm (20 000–33 300 cm^{-1}) region, but their exact peak energies

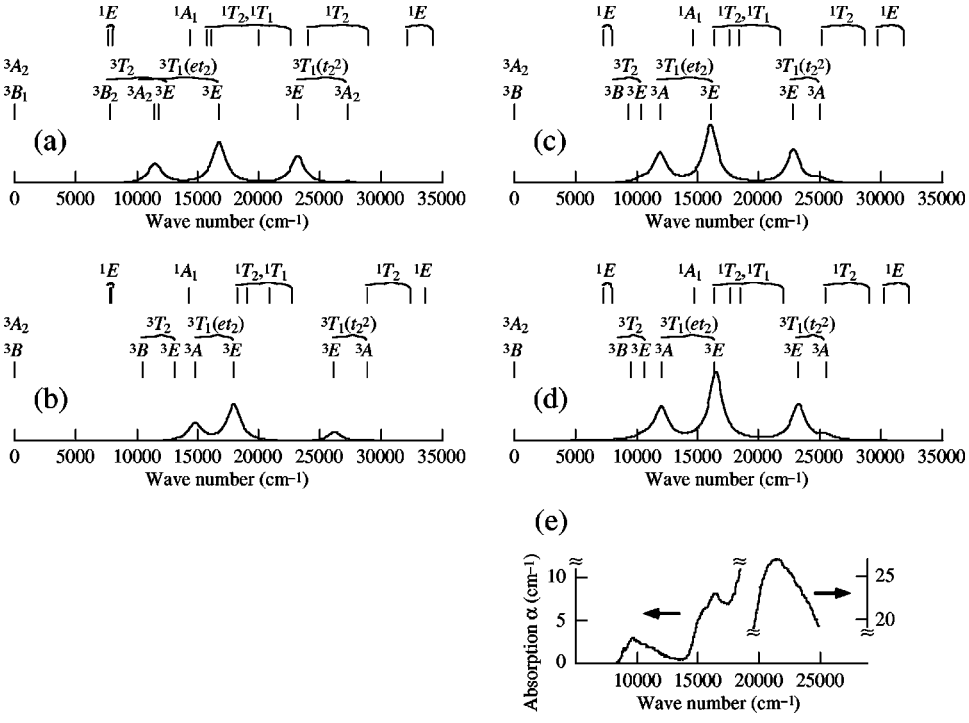

FIG. 6. (a)–(d) The calculated multiplet energies and the theoretical absorption spectra obtained from models (a)–(d) by the CIC approach. (e) The experimentally obtained absorption spectrum taken from Ref. 4 for comparison.

could not be determined exactly due to the overlap of the broad 22 200 cm^{-1} band, whose origin is yet unknown.

First, we discuss the dependence of the calculated results on the size of the cluster models. From Figs. 4, 5, and 6, we can determine that the calculated results changed as we go through models (a), (b), and (c), but the results of models (c) and (d) had no significant difference between them. Those tendencies were already indicated in the previous section by the analyses for the covalency. The energy splittings of model (a) were simply derived from the ligand field with the low D_{2d} symmetry, which was expressed by the uniaxial elongation of the CrO_4 tetrahedron. Comparing the energies obtained from models (a) and (b), we see that the energy splittings within the parent multiplet terms were smaller in model (b). The effective Madelung potential in model (b) affected the impurity-level MOs, and reduced the effect of the uniaxial elongation. In model (b), the overall energies of the triplet states were more highly estimated than the others. Moving to the larger model (c), we see that those energies were reduced. Since the mean energies of the triplet states depend on the electron configuration, the dependence of the energies on the size of the cluster models was derived from the difference in the magnitude of the effective ligand-field splitting Δ_{eff}, whose values were shown in the previous section. The values of models (a) and (c) were almost the same, on the other hand, the value of model (b) was larger than the other. The point charges around the clusters in models (b) and (c) tended to increase the magnitude of the Δ_{eff}, however on the other hand, the additional atoms around the CrO_4 tetrahedron in model (c) tended to decrease. In the results of model (a), we consider that the neglect of both the effect of the effective Madelung potential and the effect of the wave functions of the first-shell coordination polyhedra fortunately resemble the results of model (c). We should note that the resemblance was broken when we also discussed the polarization dependence of the peak intensity in the absorption spectrum of Cr^{4+}:$Ca_2MgSi_2O_7$,[39] whose crystal belonged to the tetragonal system, not the cubic system. Considering the conclusion on the covalency in the previous section together, we regard model (c) as the minimum model appropriate for the multiplet calculation.

Hereafter, we compare the three approaches: the FCZ, the CDC, and the CIC. In the results obtained by the FCZ approach in Fig. 4, the energy splittings within the parent multiplet terms were small, so that the energy structure in the parent T_d symmetry was well resolved. This result corresponds to what the framework of the FCZ approach shows: the level splitting is regarded as the splitting from the mean energy of the electron configuration, which is based on the energy structure in the parent symmetry. Comparing the theoretical spectra with the experimentally obtained absorption spectrum in Fig. 6(e), however, we see that the calculated energy structure was invalid. In the theoretical spectra, only one band was obtained in the region up to 18 000 cm^{-1}, whereas the experimentally obtained spectrum had two bands, one of which was the NIR band.

The results, which were obtained by the CDC and the CIC approaches in Figs. 5 and 6, respectively, remarkably changed from ones obtained by the FCZ approach. The energy splittings within each multiplet term became larger. It became difficult to simply assign the singlet states to the multiplet terms under the expression of the parent T_d symmetry. In the results obtained from model (a), the energies of the ^3E state in the $^3T_2$ triplet term and the $^3A_2$ state in the $^3T_1(et_2)$ triplet term crossed. When we placed point charges around the clusters in models (b), (c), and (d), the crossings were not obtained, but the large energy splittings were kept, especially on the $^3T_1(et_2)$ triplet term. The large energy splittings within the $^3T_1(et_2)$ triplet term produced the two bands in the region up to 18 000 cm^{-1}: one lay in the NIR region and the other in the visible. This energy structure corresponded to the experimentally obtained one in Fig. 6(e). The calculated oscillator strength for the NIR band was just a half of the visible band by the CIC approach. This intensity ratio agreed with the experimentally deduced ratio of the absorption coefficient, 3.6 and 7.4, for the 10 000 and the 15 400 cm^{-1} bands, respectively.[40] On the other hand, the transitions to the states in the $^3T_2$ triplet term, which were originally electric-dipole forbidden in the T_d symmetry, still did not have enough significant transition probability to produce the NIR band, although the symmetry was low. By those results, we attribute the NIR band at about 10 000 cm^{-1} and the visible band at about 15 400 cm^{-1} in the experimentally obtained spectrum to the transitions from the $^3B[^3A_2]$ ground state to the $^3A[^3T_1(et_2)]$ and the $^3E[^3T_1(et_2)]$ excited states, respectively. This assignment is consistent with the conclusion obtained by Eilers *et al.* from experiments.[13] We confirmed from first principles that the newer Eilers' assignment was valid at least regarding that the energy splitting within the $^3T_1(et_2)$ triplet term was large enough to be able to produce the NIR band.

In the original paper of the FCZ approach, Fazzio *et al.* intensively performed the systematic calculations on the multiplet structures of several transition-metal-doped semiconductors from first principles.[31] Their discussion then was almost sufficient to only show the mean energies of the multiplet terms. Furthermore, they did not discuss the transition probability. Our results from the FCZ approach showed, however, that it could not work well when the energy splittings within the multiplet terms due to the ligand field with the low symmetry became large enough to break the simple view under the parent T_d symmetry. In the CDC and the CIC approaches, we directly estimated the off-diagonal matrix elements concerning the one-electron operator term in the effective many-electron Hamiltonian. As a result, those approaches gave the proper ligand-field splittings in the low S_4 symmetry.

We consider that the CIC approach was the most reasonable approach among the three approaches when we also concentrate on the intensity ratio, although the magnitude of the energy splittings would be underestimated, compared to the CDC approach. Although we could not come to a definite conclusion from the comparison with the experimentally obtained spectrum due to the presence of the unknown broad band at 22 200 cm^{-1}, we consider that the transition probability of the transitions to the states in the $^3T_1(t_2^2)$ triplet term will not exceed those of the states in the $^3T_1(et_2)$ triplet term. This assumption is ascribed to the fact that the transi-

TABLE III. The calculated energy, the magnitude of the spin-orbit splitting, and the oscillator strength of the transitions, obtained from model (c) by the CIC approach under the relativistic calculation.

Parent state	Spin-orbit state	Energy (cm^{-1})	Spin-orbit splitting (cm^{-1})	Oscillator strength
$^3B[^3A_2(e^2)]$	Γ_3,Γ_4	⋯	0.5	⋯
⋯	Γ_2	0.5	⋯	0
$^3B[^3T_2(et_2)]$	Γ_3,Γ_4	9209	28	3×10^{-7}
⋯	Γ_2	9231	⋯	2×10^{-7}
$^3E[^3T_2(et_2)]$	$\Gamma_1(\times2)$, $\Gamma_2(\times2)$, Γ_3,Γ_4	10 317–10 414	97	1×10^{-4}
$^3A[^3T_1(et_2)]$	Γ_3,Γ_4	11 896	6	27×10^{-4}
⋯	Γ_1	11 902	⋯	26×10^{-4}
$^3E[^3T_1(et_2)]$	$\Gamma_1(\times2)$, $\Gamma_2(\times2)$, Γ_3,Γ_4	15 975–16 109	134	28×10^{-4}
$^1A[^1E(e^2)]$	Γ_1	7385	⋯	3×10^{-6}
$^1B[^1E(e^2)]$	Γ_2	8047	⋯	1×10^{-6}
$^1A[^1A_1(e^2)]$	Γ_1	14 685	⋯	5×10^{-5}

tion probability concerning the two-electron excitation originates only from the mixing of the wave functions concerning the one-electron-excited electron configuration. Further discussion on the relationship between the transition probability and the mixing of the wave functions will be shown in Sec. III B 4. In Fig. 5 by the CDC approach, we find that the transitions to the $^3E[^3T_1(t_2^2)]$ state were stronger than ones to the $^3E[^3T_1(et_2)]$ state [except for the result of model (b)]. Therefore we regard the results obtained by the CDC approach as unreasonable ones, only shifting the diagonal matrix elements caused the interactions between the states in the different electron configurations to break. In the ruby's case, where the multiplet structure in the parent symmetry was resolved well, the CDC approach gave the appropriate results.[26] However, in the case of the tetrahedrally coordinated Cr^{4+} in the YAG, where the ligand field splitting that originated from the low S_4 symmetry also dominated the multiplet structure, the CDC approach was not a perfect one. In the CIC approach, where all the matrix elements concerning the one-electron operator term were corrected, the transition probabilities of the $^3B[^3A_2]\rightarrow{}^3E[^3T_1(t_2^2)]$ transitions were smaller than those of the $^3B[^3A_2]\rightarrow{}^3E[^3T_1(et_2)]$ transitions in every cluster model, as shown in Fig. 6.

2. The assignment of the peaks in the absorption spectrum

In this subsection, we discuss the validity of the assignment of the peaks in the absorption spectrum written in the literature. We discuss the results obtained from the fully relativistic calculation, including the spin-orbit interaction. The calculated energy, the magnitude of the spin-orbit splitting, and the oscillator strength of the transitions, obtained from model (c) by the CIC approach, are summarized in Table III. We had confirmed that the energy and the theoretical spectrum, obtained by the relativistic calculation, were consistent as a whole with those obtained by the nonrelativistic calculation. We can consider that the only difference in the relativistic result was the existence of the spin-orbit splitting, and the existence of the transition probability of the spin-forbidden transitions. In the CIC approach, the magnitude of the energy splitting, derived from the ligand field under the low S_4 symmetry, would be underestimated, compared to the result of the CDC approach. However, the underestimation will not affect the discussion by the order of magnitude. Although the other overestimation and underestimation concerning the calculated energies might be involved, we consider that rough estimations of the magnitude of the energy splittings and the oscillator strength of the transitions can be done. To specify a state with symmetry symbols, we used the Mulliken symbol for the parent state under the nonrelativistic representation; on the other hand, we used Bethe's symbol for the spin-orbit state under the relativistic representation.

First, we focus on the spin-orbit splitting of the $^3B[^3A_2(e^2)]$ ground state. The ground state split into the three spin-orbit states, Γ_3, Γ_4, and Γ_2 under the S_4 symmetry. The Γ_3 and Γ_4 spin-orbit states were almost degenerate. Therefore the magnitude of the spin-orbit splitting was regarded as the energy difference between the $(\Gamma_3+\Gamma_4)$ states and the Γ_2 state. The value of the spin-orbit splitting was $0.5\,cm^{-1}$. Kück *et al.* assumed the value to be $2\,cm^{-1}$,[4] referring to the value obtained for Cr^{4+}:Mg_2SiO_4 in the literature. Our calculated value was smaller by only a factor of 1/4, supporting Kück's magnitude. We expect from the result that the magnitude of the spin-orbit splitting of the $^3B[^3A_2(e^2)]$ ground state was so small that both the states would be thermally populated. Therefore, we considered all the transitions from the three spin-orbit states for the calculation of the oscillator strength of the ground-state absorption.

The spin-orbit splitting of the $^3B[^3T_2(et_2)]$ state was $28\,cm^{-1}$. Here also, the Γ_3 and Γ_4 spin-orbit states were almost degenerate. The oscillator strengths of the $^3B[^3A_2(e^2)]\rightarrow{}^3B[^3T_2(et_2)]$ transitions were 2×10^{-7}–3×10^{-7}. Those were at least 4 orders of magnitude smaller than the values concerning the $^3T_1(et_2)$ triplet term. The small oscillator strength is ascribed to the transitions to the $^3B[^3T_2(et_2)]$ states being allowed only by the spin-orbit interaction. When we neglect the small spin-orbit splitting of the ground state, we can expect that a zero-phonon line with a doublet structure will be observed in the experimentally obtained absorption spectrum. Actually, the doublet zero-phonon lines peaking at 7814 and $7842\,cm^{-1}$, with the energy splitting of $28\,cm^{-1}$, had already been considered to have originated from the transitions to the spin-orbit states of the $^3B[^3T_2(et_2)]$ state,[4,11,13–16] as shown in Table I. The

assignment seems reasonable. Still we could not completely omit the possibility of assigning those peaks to the other absorption centers. One possibility is the tetrahedrally coordinated Cr^{4+} coupling with a codopant atom for charge compensation, and the effect of the Cr–Ca pair will be discussed in the next subsection. Another possibility is the $^2B[^2E] \rightarrow {}^2B[^2T_2]$ transition of the tetrahedrally coordinated Cr^{5+}, whose resemblance to the transition of the Cr^{4+} state was pointed out in our recent study.[41]

The $^3E[^3T_2(et_2)]$ state split into six spin-orbit states under the S_4 symmetry. In this case, the Γ_3 and the Γ_4 spin-orbit states had apparent energy splitting with more than $1\,cm^{-1}$. The energy difference between the highest and the lowest spin-orbit states was $97\,cm^{-1}$. Borodin *et al.*[8] and Okhrimchuk and Shestakov[12] assigned the two sharp lines at 8977 and $9281\,cm^{-1}$ to the transitions to the spin-orbit components of the $^3E[^3T_2(et_2)]$ states. Kück *et al.* also negatively mentioned the same possibility.[11] However, we omit their possibility, because no additional peak existed between the two lines with the large energy difference: $304\,cm^{-1}$. It is unlikely that the two lines originated from the nearest spin-orbit states. The oscillator strengths of the six transitions were about 1×10^{-4} for each. The magnitude was only an order smaller than the transitions to the $^3A[^3T_1(et_2)]$ states. The peaks concerning the $^3E[^3T_2(et_2)]$ states have been considered hidden under the broad band at around $10\,000\,cm^{-1}$, which has been attributed to the transition to the $^3A[^3T_1(et_2)]$ state.[13] Kück *et al.* attributed several apparent peaks in the $9463–10\,392\,cm^{-1}$ region under a low temperature to the phonon-related transitions.[4] However, we consider that some of those peaks could be attributed to the transitions to the spin-orbit states in the $^3E[^3T_2(et_2)]$ state, since the calculated oscillator strength was large enough to allow the peaks to be observed.

The $^1E(e^2)$ singlet term split into the lower Γ_1 state and the higher Γ_2 state by the ligand field under the S_4 symmetry. The calculated peak positions should be underestimated, depending on the accuracy in the estimation of the magnitude of the correlation-correction factor C, which shifted the energies as a whole. We had confirmed, however, that the discussion below, on the magnitude of the ligand-field splitting and the oscillator strength, was insensitive to the energy position by examining the dependence of the energy splitting on the correlation-correction factor. From Table III, we see that the magnitude of the ligand-field splitting of the $^1E(e^2)$ singlet term was $662\,cm^{-1}$ by the CIC approach. The splitting obtained by the CDC approach was $1290\,cm^{-1}$. Although the magnitude of the ligand-field splitting by the CIC approach was likely to be underestimated, we can say that the magnitude should not be smaller at least than $662\,cm^{-1}$. Eilers *et al.* tentatively assigned the two lines at 1210 nm ($8264\,cm^{-1}$) and 1206 nm ($8292\,cm^{-1}$), with the energy splitting of $28\,cm^{-1}$ to the transitions to the states of the $^1E(e^2)$ singlet term.[13] Riley *et al.* pointed out by the semiempirical AOM calculation that the splitting would be at least $1000\,cm^{-1}$, and that the Eilers' assignment should be wrong.[16] We agree with Riley's conclusion. The oscillator strength of the transition to the Γ_1 state was 5×10^{-5}, whose magnitude was not small, and comparable to the magnitude concerning the $^3E[^3T_2(et_2)]$ states. We consider that an apparent peak, originating from the transition to the Γ_1 state of the $^1E(e^2)$ singlet term, could be observed in the absorption spectrum.

In the previous subsection, we had already confirmed that the ligand-field splitting of the $^3T_1(et_2)$ triplet term was large enough to produce both the NIR and the visible bands. We consider further the magnitude of the spin-orbit splitting of the $^3A[^3T_1(et_2)]$ state, which corresponds to the NIR band. The $^3A[^3T_1(et_2)]$ state split into the three spin-orbit states, Γ_3, Γ_4, and Γ_1, under the S_4 symmetry. The energy difference between the Γ_3 and the Γ_4 spin-orbit states was negligibly smaller than $1\,cm^{-1}$, hence we can again regard those states as a degenerate state. The calculated magnitude of the spin-orbit splitting between the $(\Gamma_3+\Gamma_4)$ states and the Γ_1 state was only $6\,cm^{-1}$. This small spin-orbit splitting contradicts the assignment (or the assumption) proposed by Kück *et al.*,[4] Riley *et al.*,[16] and Henderson *et al.*[17] They considered that the two intense lines at 8977 and $9281\,cm^{-1}$, with the energy separation of $304\,cm^{-1}$, originated from the transitions to the Γ_1 and the $(\Gamma_3+\Gamma_4)$ spin-orbit states, respectively. Their assignment, however, would also contradict the conclusion obtained by Eilers *et al.*, who pointed out that the two lines should have the same polarization dependence, and that the line at $9281\,cm^{-1}$ might have originated from the vibrational mode.[13] Before the Eilers' suggestion, Kück *et al.* mentioned that the two lines originated from the transitions to the $^1E(e^2)$ states, which split by the ligand field under the S_4 symmetry.[11] But the assignment would also not satisfy the Eilers' requirement, because the two states have different symmetry, Γ_1 and Γ_2. The contradiction on the assignment of the two intense lines at 8977 and $9281\,cm^{-1}$ would not be solved yet. We consider that one possible explanation would still be the Eilers' one. Another possible explanation may be that the 8977 and the $9281\,cm^{-1}$ lines are differently attributed to the $^3B[^3A_2(e^2)] \rightarrow {}^1A[^1E(e^2)]$ and the $^3B[^3A_2(e^2)] \rightarrow {}^3A[^3T_1(et_2)]$ transitions, respectively. If the magnitude of the spin-orbit splitting of the $^3A[^3T_1(et_2)]$ state is significantly larger than that obtained by us, the spin-orbit states will have different symmetries, and we have to find the corresponding additional peaks somewhere in the broad band for the different polarization to explain Eilers' results on the polarization dependence under the uniaxial stress.

The $^3E[^3T_1(et_2)]$ state in the visible region also split into the six spin-orbit states. The energy difference between the highest and the lowest states was $134\,cm^{-1}$. It is known that the broad band at around $15\,400\,cm^{-1}$ possessed an apparent shoulder.[13] We consider that such a structure did not originate from the spin-orbit splitting of the $^3E[^3T_1(et_2)]$ state, since the magnitude of the spin-orbit splitting was too small to be apparently distinguished in the broad band. The structure could be attributed to the Cr^{4+} coupling with codopant atoms.

3. The effect of the Cr–Ca pair

The existence of the charge compensators, such as Ca or Mg atoms, makes it difficult to analyze the absorption spectrum of Cr^{4+}:YAG. Okhrimchuk and Shestakov showed by

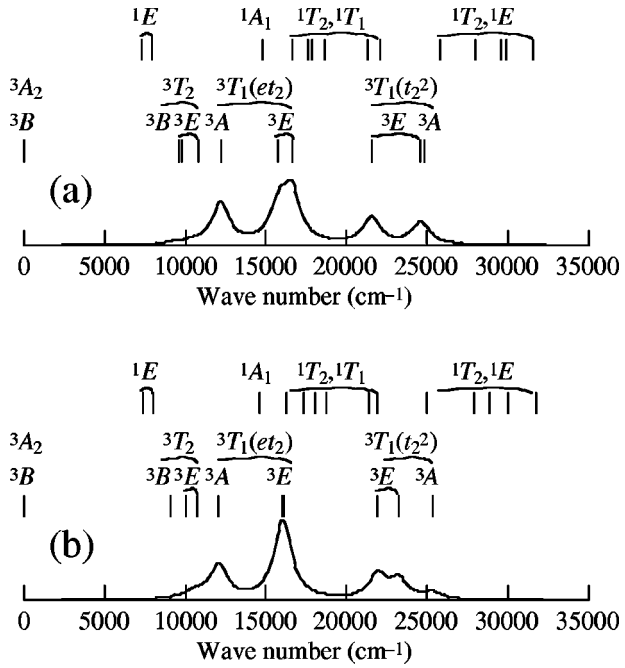

FIG. 7. (a), (b) The calculated multiplet energies and the theoretical absorption spectra obtained from models (e) and (f) by the CIC approach. The symmetry symbols are approximated by those of the parent S_4 symmetry.

the experiments that the absorption cross section of the peak at 7800 cm^{-1} decreased by 6 orders of magnitude, when the concentration of the Cr atoms increased by a factor of 13 and the concentration of the Mg atoms decreased by a factor of 4.3.[12] Under the same condition, the absorption cross section of the peak at 8100 cm^{-1} did not show any significant change. They attributed the peak at 7800 cm^{-1} to a different absorption center rather than the dominant tetrahedrally coordinated Cr^{4+}. This indicates that the determination of the assignment of the peaks in the absorption spectrum is not straightforward. It is difficult to discuss theoretically the chemical state coupling with the codopants, because the problem involves ion–ion interaction, which has been omitted in the framework of the traditional ligand-field analyses. We can find, however, some literature that considered the effect of the codopants by some theoretical calculations. Kuklja calculated the formation energies of the defects in the YAG by the classical model using pair potentials.[42] Sobolev *et al.* insisted the importance of the Cr–Ca pair by their electronic-structure calculation.[20] And Ching *et al.* tried to explain the mechanism of the saturable absorption by their band calculation including the Cr–Ca pairs.[22] But none have directly discussed the effect of the codopants on the structure of the absorption spectrum.

We estimated the maximum effect of the Cr–Ca pair on the absorption spectrum. Hereafter, we return to the results obtained by the nonrelativistic calculations. The calculated multiplet energies and the theoretical spectra, obtained from models (e) and (f) by the CIC approach, are shown in Figs. 7(a) and 7(b). We see from the results that the ^3E states further split into two states, which created additional peaks and shoulders in the spectra. (The symmetry symbols were approximated by those of the S_4 parent symmetry.) Although

TABLE IV. The calculated oscillator strengths ($\times 10^{-4}$), obtained from models (c), (e), and (f) by the CIC approach under the nonrelativistic calculation.

Model (c)	$^3B[^3T_2]$	0
	$^3E[^3T_2]$	6
	$^3A[^3T_1(et_2)]$	70
	$^3E[^3T_1(et_2)]$	144
Model (e)	$^3B_{(1)}[^3T_2]$	3
	$^3A_{(2)}[^3T_2]$	1
	$^3B_{(3)}[^3T_2]$	3
	$^3A_{(4)}[^3T_1(et_2)]$	72
	$^3B_{(5)}[^3T_1(et_2)]$	60
	$^3B_{(6)}[^3T_1(et_2)]$	89
Model (f)	$^3A_{(1)}[^3T_2]$	0
	$^3A_{(2)}[^3T_2]$	3
	$^3A_{(3)}[^3T_2]$	10
	$^3A_{(4)}[^3T_1(et_2)]$	61
	$^3A_{(5)}[^3T_1(et_2)]$	78
	$^3A_{(6)}[^3T_1(et_2)]$	64

the energy splitting of the $^3E[^3T_1(t_2^2)]$ parent states produced the apparent changes above 20 000 cm^{-1}, they will not be observed in the experimentally obtained absorption spectrum due to the intense band at around 22 200 cm^{-1}. On the other hand, we can expect that the energy splitting of the $^3E[^3T_2]$ parent states will create some satellite peaks in the NIR region. Some calculated oscillator strengths of models (e) and (f) with a Ca atom by the CIC approach are summarized in Table IV, besides the result of the model (c) without the Ca atom. In the result obtained from model (e), we see that the $^3A_{(2)}[^3T_2]$ state, which corresponded to the $^3B[^3T_2]$ state in model (c), had an apparent transition probability, 1×10^{-4}. Although the transition to the $^3B[^3T_2]$ state under the S_4 symmetry was electric-dipole forbidden, the transition became allowed when the symmetry was reduced to C_2. In the result obtained from model (f), the oscillator strength of the transition to the $^3A_{(1)}[^3T_2]$ state, which corresponded to the $^3B[^3T_2]$ state in model (c), did not show any significant increase. Instead, the transition to the $^3A_{(3)}[^3T_2]$ state originating from the $^3E[^3T_2]$ parent state was twice strengthened. In either case of the nearest Cr–Ca pair, the increase of the absorption coefficient of some related peaks is expected to be observed in the NIR region in the experimentally observed spectrum, followed by the increase of the concentration of the Ca atoms. The concentration-dependent zero-phonon lines at about 7800 cm^{-1} in the experimentally obtained spectrum may have originated from the tetrahedrally coordinated Cr^{4+} coupling with a Ca atom. Regarding the $^3E[^3T_1(et_2)]$ parent state, we see that the energy splitting of model (e) in Fig. 7(a) created an apparent doublet structure in the spectrum. This indicates that the shoulder observed in the 15 400 cm^{-1} band could have originated from the Cr–Ca pair.

4. The relationship between the transition probability and the mixing of wave functions

The magnitude of the calculated oscillator strength is related to the results of the analysis of the coefficients C_{ij} in Eq. (2). The summarized coefficients in the wave functions

TABLE V. The summarized coefficients C_{ij} in the linear combination of Slater determinants Φ^a in Eq. (2) obtained from cluster model (c) by the CIC approach under the nonrelativistic calculation. The matrix elements that are not filled are considered to be zero. The overline in the labels of the Slater determinants means to take an average value concerning the two determinants.

	(et_2)				(t_2^2)	
States Ψ	Φ_1	$\Phi_{\overline{2+3}}$	Φ_4	$\Phi_{\overline{5+6}}$	$\Phi_{\overline{7+8}}$	Φ_9
$^3B[^3T_2(et_2)]$	1.00	⋯	⋯	⋯	⋯	⋯
$^3E[^3T_2(et_2)]$	⋯	0.88	⋯	0.11	⋯	⋯
$^3A[^3T_1(et_2)]$	⋯	⋯	0.94	⋯	⋯	0.06
$^3E[^3T_1(et_2)]$	⋯	0.07	⋯	0.66	0.27	⋯
$^3E[^3T_1(t_2^2)]$	⋯	0.05	⋯	0.23	0.72	⋯
$^3A[^3T_1(t_2^2)]$	⋯	⋯	0.06	⋯	⋯	0.94

[a] $\Phi_1=|a_{(2)}(e),b_{(3)}(t_2)|$, $\Phi_2=|b_{(3)}(e),e_{(5)}(t_2)|$, $\Phi_3=|b_{(3)}(e),e_{(4)}(t_2)|$, $\Phi_4=|b_{(3)}(e),b_{(3)}(t_2)|$,
$\Phi_5=|a_{(2)}(e),e_{(5)}(t_2)|$, $\Phi_6=|a_{(2)}(e),e_{(4)}(t_2)|$, $\Phi_7=|b_{(3)}(t_2),e_{(5)}(t_2)|$, $\Phi_8=|b_{(3)}(t_2),e_{(4)}(t_2)|$,
$\Phi_9=|e_{(5)}(t_2),e_{(4)}(t_2)|$, where $|\varphi_1,\varphi_2|=1/\sqrt{2}\{\varphi_1(\mathbf{r}_1)\varphi_2(\mathbf{r}_2)-\varphi_2(\mathbf{r}_1)\varphi_1(\mathbf{r}_2)\}$.

Ψ of the excited triplet states, obtained from model (c) by the CIC approach [corresponding to Fig. 6(c)], are shown in Table V. The values were normalized by unity, and the empty elements indicated zero. Every line in Table V shows the composition of the state, and the off-diagonal elements mean that the wave function of the state was mixed with the wave functions of the other states. Originally, in the parent T_d symmetry, the wave functions of the $^3T_2(et_2)$ state are the Slater determinants Φ_1, Φ_2, and Φ_3, and have no off-diagonal elements. All the Slater determinants $\Phi_1-\Phi_6$ were composed of an MO originating from e symmetry and another MO originating from t_2 symmetry, and belonged to the et_2 electron configuration. On the other hand, the Slater determinants $\Phi_7-\Phi_9$ were composed of the two MOs both originating from t_2 symmetry, and belonged to the t_2^2 electron configuration.

First, we discuss the states in the $^3T_1(t_2^2)$ triplet term. Originally, the optical transition involving two-electron excitation is forbidden. However, some transitions to the states in the $^3T_1(t_2^2)$ triplet term had the transition probabilities. In Table V, we see that the wave function of the $^3A[^3T_1(t_2^2)]$ state almost preserved its own character, expressed by the contribution of the Slater determinant $\Phi_9(t_2^2)$ at 0.94. On the other hand, the wave function of the $^3E[^3T_1(t_2^2)]$ state reduced its own character $\Phi_{\overline{7+8}}(t_2^2)$ to 0.72 by mixing with $\Phi_{\overline{5+6}}(et_2)$, which was the main component of the wave function of the $^3E[^3T_1(et_2)]$ state. We find correspondence between those magnitudes of the mixing of the wave functions and the magnitude of the transition probability shown in Fig. 6(c). The larger the mixing was, the larger the transition probability was. We conclude that the transition probability of the transitions to the states in the t_2^2 electron configuration was produced by mixing of the wave functions with those of the states in the et_2 electron configuration.

Regarding the $^3B[^3T_2(et_2)]$ state in the NIR region, the peak intensity in the experimentally obtained absorption spectrum should be considerably weak. The $^3B[^3A_2]\rightarrow{}^3B[^3T_2(et_2)]$ transition in the S_4 symmetry was still electric-dipole forbidden, and the $^3B[^3T_2(et_2)]$ state was the only excited state having the B symmetry. This situation resulted in the absence of the interaction of the $^3B[^3T_2(et_2)]$ state with the other triplet states, expressed by the diagonal value 1.00 in Table V. As shown in Sec. III B 2, the transition probability came only from the spin-orbit interaction. On the other hand, the $^3E[^3T_2(et_2)]$ state had the value of the off-diagonal elements, 0.11, for the interaction with the $^3E[^3T_1(et_2)]$ state through the Slater determinant $\Phi_{\overline{5+6}}$. In the theoretical spectrum in Fig. 6(c), the peak intensity corresponding to the transition to the $^3E[^3T_2(et_2)]$ state was indeed observed.

5. The reduction factors on electron repulsion

The electron repulsion of an ion in solids or complexes is largely reduced from that of a gaseous free ion. In the framework of the crystal field theory or the ligand field theory, the Racah parameter B has usually been regarded as the single parameter expressing the electron repulsion that concerns the multiplet structure. The magnitude of the reduction of the electron repulsion has been estimated by the so-called nephelauxetic parameter, which is a ratio of the Racah parameter B in the ligand field to the free ion.[43]

In the DVME method, the reduction is expressed by the degree of covalency and by the correlation-correction factor C. The calculated correlation-correction factor C, obtained from models (a)–(d) by the FCZ, the CDC, and the CIC approaches, are listed in Table VI, where the value obtained from the Cr^{4+} free-ion model is also shown. We see that the dependence of the correlation-correction factor on the approaches was negligibly small. As for the dependence on the cluster models, we see that the result of model (b) was smaller than the results of the other models. The correlation-correction factor of models (c) and (d) were almost the same.

TABLE VI. The calculated correlation-correction factor C in Eq. (5), obtained from models (a)–(d) by the FCZ, the CDC, and the CIC approaches, and from the free-ion model.

Models	FCZ	CDC	CIC
(a)	0.65	0.67	0.65
(b)	0.60	0.60	0.59
(c)	0.68	0.69	0.68
(d)	0.69	0.70	0.69
Free ion		0.89	

TABLE VII. The multiplied reduction factor, obtained from the models (a)–(d) by the FCZ, the CDC, and the CIC approaches.

Models	FCZ	CDC	CIC
(a)	0.50	0.52	0.50
(b)	0.48	0.48	0.47
(c)	0.52	0.53	0.52
(d)	0.52	0.53	0.52

We find a contrary tendency to the results of the covalency in Table II: the smaller values were obtained for the factor C, as the larger values of the proportions of the contribution of the Cr $3d$ orbitals were obtained. We consider that the multiplication of the two reduction factors corresponds to the meaning of the nephelauxetic effect. Multiplying the correlation-correction factor C in Table VI and the mean values of the contributions of the Cr $3d$ orbitals in Table II together, we obtained the multiplied reduction factor, listed in Table VII. The values lay within the range from 0.47 to 0.53. The multiplied reduction factor is a convenient indication to show the degree of reduction of the electron repulsion.

The direct estimation of the electron repulsion was done by calculating directly the ratio corresponding to the traditional nephelauxetic parameter. For simplification, we considered only the representative two-electron integrals, $\langle ij|kl\rangle = \langle 11|11\rangle$, $\langle 22|22\rangle$, $\langle 33|33\rangle$, $\langle 44|44\rangle$ in Eq. (5), where Figs. 1–4 specify the four impurity-level MOs. In those four integrals, the difference in the covalency was already involved. The values of the two-electron integrals that were multiplied by the correlation-correction factor C are listed in Table VIII for model (c) and for the free-ion model. Comparing the results with those of the covalency in Table II(c), we see that the magnitude of the two-electron integrals decreased as the degree of covalency increased. Contrary to the traditional methods that reduced the number of parameters for the two-electron integrals to only one, our method directly gave the difference of the two-electron integrals, according to the difference of the covalency under the S_4 symmetry. Considering that the fourth state was twofold degenerate, we obtained the mean value of the two-electron integrals at 11.9 eV. The corresponding value, obtained from the Cr^{4+} free-ion model, was 23.2 eV. Applying those values to the definition of the nephelauxetic parameter, we obtained the nephelauxetic parameter at 0.51. Eilers, Brik, and Riley independently obtained the values of the Racah parameter B by their semiempirical analyses at 515, 500, and 430 cm^{-1}, respectively.[13,15,16] They correspond to the value of the nephelauxetic parameter in the range from 0.42 to 0.51, and the magnitude seems to be supported now generally for the tetrahedrally coordinated Cr^{4+} state. Our value agreed especially with the Eilers' and the Brik's ones. Thus, we confirmed from first principles that those experimentally deduced values of the nephelauxetic parameter had the appropriate magnitude.

TABLE VIII. The values of the representative two-electron integrals multiplied by the correlation-correction factor C (eV), obtained from the model (c) by the CIC approach, and the free-ion model.

$\langle ij\|kl\rangle$	Model (c)	Free-ion model
$\langle 11\|11\rangle$	12.8	
$\langle 22\|22\rangle$	12.3	
$\langle 33\|33\rangle$	11.5	
$\langle 44\|44\rangle$	11.4	
Average	11.9	23.2

IV. SUMMARY

The multiplet structure of the tetrahedrally coordinated Cr^{4+} in YAG was calculated by the *ab initio* many-electron calculation method, developed by us. We revealed that the wave functions of the cations outside the CrO_4 tetrahedron also affected the covalency of the impurity-level molecular orbitals. We concluded that the model with the first-shell coordination polyhedra was required. We confirmed that the $^3T_1(et_2)$ triplet term should have the large ligand-field splitting, which created both the NIR and the visible bands, supporting the earlier Eilers' suggestion.[13] To discuss the possible assignments, we conducted the calculation by the fully relativistic many-electron calculation method. The magnitudes of the spin-orbit and the ligand-field splittings, and the oscillator strength of the transitions were discussed. We estimated the traditional nephelauxetic parameter from first principles. The calculated nephelauxetic parameter was 0.51, which supported the magnitude of the parameter reported in some literature.

Until now, the Ca or Mg atom has been codoped only for the purpose of achieving the charge compensation, and of stabilizing the Cr^{4+} state. Our results indicated, however, that the formation of the nearest Cr–Ca pairs would create some additional peaks in the absorption spectrum. This means that the codopants can be regarded not only as a charge compensator, but also as a modifier of the wavelength and the cross section of the absorption and the emission. Shen and Bray recently mentioned that controlling the local distortion around the transition-metal centers would lead to the design of new optical materials.[44] We support their direction. However, we consider that the meaning of the ''distortion'' should also include the recombination of the wave functions that change the covalency. Such a discussion on the covalency, involving the ion–ion interaction, requires us to investigate with larger models than the model with only a few ligand atoms. We believe that to design the solid-state laser materials from first-principles calculation is possible when we systematically examine the effect of various codopants, with large models directly involving the ion–ion interaction.

ACKNOWLEDGMENTS

This study was supported by a Grant-in-Aid for Scientific Research from the Ministry of Education, Sports, and Culture of Japan. One of the authors (T.I.) is a Research Fellow of the Japan Society for the Promotion of Science (JSPS Research Fellow).

[1] V. Petričević, S. K. Gayen, R. R. Alfano, K. Yamagishi, H. Anzai, and Y. Yamaguchi, Appl. Phys. Lett. **52**, 1040 (1988); V. Petričević, S. K. Gayen, and R. R. Alfano, *ibid.* **53**, 2590 (1988); H. R. Verdun, L. M. Thomas, D. M. Andrauskas, T. McCollum, and A. Pinto, *ibid.* **53**, 2593 (1988).
[2] A. P. Shkadarevich, in *OSA Proceedings on Tunable Solid State Lasers, 1989*, edited by M. L. Shand and H. P. Jenssen (Optical Society of America, Washington, DC, 1989), Vol. 5, p. 60.
[3] S. Kück, K. Petermann, U. Pohlmann, and G. Huber, Phys. Rev. B **51**, 17323 (1995).
[4] S. Kück, K. Petermann, U. Pohlmann, and G. Huber, J. Lumin. **68**, 1 (1996).
[5] Y. Kalisky, A. B.-A. Baranga, Y. Shimony, and M. R. Kokta, Opt. Mater. **8**, 129 (1997).
[6] A. G. Okhrimchuk and A. V. Shestakov, Phys. Rev. B **61**, 988 (2000).
[7] L. I. Krutova, N. A. Kulagin, V. A. Sandulenko, and A. V. Sandulenko, Fiz. Tverd. Tela (Leningrad) **31**, 170 (1989) [Sov. Phys. Solid State **31**, 1193 (1989)].
[8] N. I. Borodin, A. G. Okhrimchuk, and A. V. Shestakov, in *OSA Proceedings on Advanced Solid-State Lasers, 1992*, edited by L. L. Chase and A. A. Pinto (Optical Society of America, Washington, DC, 1992), Vol. 13, p. 42.
[9] K. R. Hoffman, U. Hömmerich, S. M. Jacobsen, and W. M. Yen, J. Lumin. **52**, 277 (1992).
[10] W. Jia, H. Liu, Y. Wang, U. Hömmerich, H. Eilers, K. Hoffman, and W. M. Yen, J. Lumin. **59**, 279 (1994).
[11] S. Kück, U. Pohlmann, K. Petermann, G. Huber, and T. Schönherr, J. Lumin. **60&61**, 192 (1994).
[12] A. G. Okhrimchuk and A. V. Shestakov, Opt. Mater. **3**, 1 (1994).
[13] H. Eilers, U. Hömmerich, S. M. Jacobsen, W. M. Yen, K. R. Hoffman, and W. Jia, Phys. Rev. B **49**, 15505 (1994).
[14] U. Hömmerich, Y. Shen, and K. Bray, J. Lumin. **72–74**, 139 (1997).
[15] M. G. Brik and D. G. Shchekoldin, Opt. Spektrosk. **84**, 760 (1998) [Opt. Spectrosc. **84**, 683 (1998)].
[16] M. J. Riley, E. R. Krausz, N. B. Manson, and B. Henderson, Phys. Rev. B **59**, 1850 (1999).
[17] B. Henderson, H. G. Gallagher, T. P. J. Han, and M. A. Scott, J. Phys.: Condens. Matter **12**, 1927 (2000).
[18] S. Sugano, Y. Tanabe, and H. Kamimura, *Multiplets of Transition-Metal Ions in Crystals* (Academic, New York, 1970).
[19] C. E. Schäffer and C. K. Jørgensen, Mol. Phys. **9**, 401 (1965).
[20] A. B. Sobolev, I. F. Bikmetov, V. A. Lobach, A. I. Mit'kovets, A. A. Stavrov, and A. P. Shkadarevich, Fiz. Tverd. Tela (Leningrad) **33**, 321 (1991) [Sov. Phys. Solid State **33**, 185 (1991)].
[21] Y.-N. Xu and W. Y. Ching, Phys. Rev. B **59**, 10530 (1999).
[22] W. Y. Ching, Y.-N. Xu, and B. K. Brickeen, Appl. Phys. Lett. **74**, 3755 (1999).
[23] K. Wissing, J. A. Aramburu, M. T. Barriuso, and M. Moreno, Solid State Commun. **108**, 1001 (1998).
[24] W. Kohn and L. J. Sham, Phys. Rev. **140**, A1133 (1965).
[25] F. Deghoul, H. Chermette, F. Rogemond, R. Moncorgé, C. Stückl, and C. Daul, Phys. Rev. B **60**, 2404 (1999).
[26] K. Ogasawara, T. Ishii, I. Tanaka, and H. Adachi, Phys. Rev. B **61**, 143 (2000).
[27] T. Ishii, K. Ogasawara, I. Tanaka, and H. Adachi, in *OSA Trends in Optics and Photonics, Advanced Solid State Lasers, 2000*, edited by H. Injeyan, U. Keller, and C. Marshall (Optical Society of America, Washington, DC, 2000), Vol. 34, p. 514.
[28] C. Satoko, M. Tsukada, and H. Adachi, J. Phys. Soc. Jpn. **45**, 1333 (1978).
[29] J. C. Slater, T. M. Wilson, and J. H. Wood, Phys. Rev. **179**, 28 (1969).
[30] J. C. Slater, *The Self-Consistent Field for Molecules and Solids, Quantum Theory of Molecules and Solids* (McGraw-Hill, New York, 1974), Vol. 4.
[31] A. Fazzio, M. J. Caldas, and A. Zunger, Phys. Rev. B **30**, 3430 (1984).
[32] S. Watanabe and H. Kamimura, Mater. Sci. Eng., B **3**, 313 (1989).
[33] J. Onoe, H. Nakamatsu, T. Mukoyama, R. Sekine, H. Adachi, and K. Takeuchi, Inorg. Chem. **36**, 1934 (1997).
[34] F. Euler and J. A. Bruce, Acta Crystallogr. **19**, 971 (1965).
[35] R. D. Shannon, Acta Crystallogr., Sect. A: Cryst. Phys., Diffr., Theor. Gen. Crystallogr. **32**, 751 (1976).
[36] G. A. Slack, D. W. Oliver, R. M. Chrenko, and S. Roberts, Phys. Rev. **177**, 1308 (1969).
[37] T. Tomiki *et al.*, J. Phys. Soc. Jpn. **65**, 1106 (1996).
[38] R. S. Mulliken, J. Chem. Phys. **23**, 1833 (1955).
[39] T. Ishii, K. Fujimura, K. Ogasawara, I. Tanaka, and H. Adachi, in *Proceedings SPIE, Laser Optics 2000: Solid-State Lasers, 2000*, edited by V. I. Ustugov (The Society of Photo-Optical Instrumentation Engineers, Washington, 2001), Vol. 4350, p. 90.
[40] S. Kück, K. Petermann, and G. Huber, in *OSA Proceedings on Advanced Solid-State Lasers, 1991*, edited by G. Dubé and L. Chase (Optical Society of America, Washington, DC, 1991), Vol. 10, p. 92.
[41] T. Ishii, K. Ogasawara, H. Adachi, and I. Tanaka, Appl. Phys. Lett. **78**, 2154 (2001).
[42] M. M. Kuklja, J. Phys.: Condens. Matter **12**, 2953 (2000).
[43] D. F. Shriver, P. W. Atkins, and C. H. Langford, *Inorganic Chemistry*, 2nd ed. (Oxford University Press, Oxford, 1994), p. 594.
[44] Y. Shen and K. L. Bray, Phys. Rev. Lett. **84**, 3990 (2000).